Montanuniversität Leoben

Sputtered $Cr_{1-x}Al_xN$ hard coatings with $0.21 \leq x \leq 0.46$

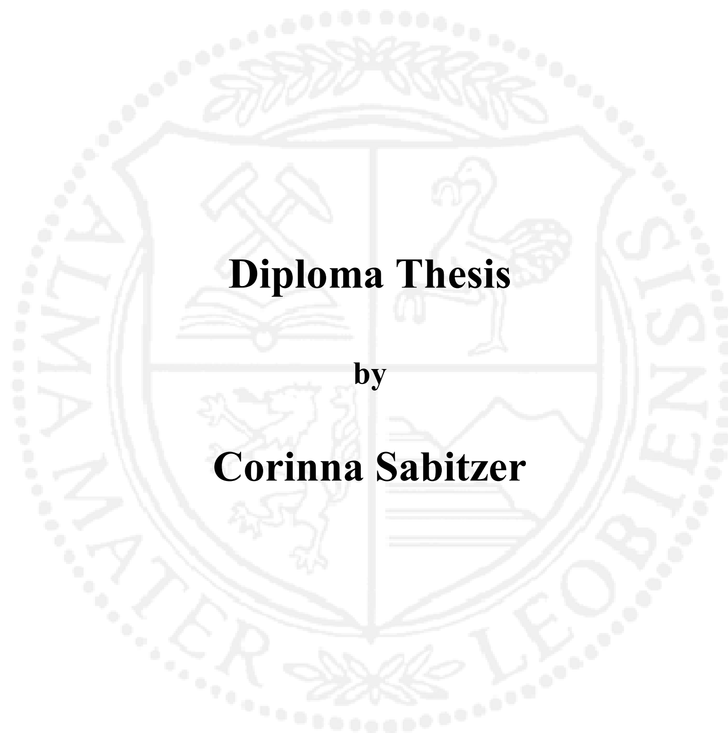

Diploma Thesis

by

Corinna Sabitzer

This work has been carried out within the Research Studio Austria Surface Engineering at the Chair of Functional Materials and Materials Systems at the University of Leoben, Austria.

Leoben, November 2011

Affidavit:

I declare in lieu of ought, that I wrote this thesis and performed the associated research myself, using only literature cited in this volume

Leoben, November 2011

Acknowledgment

I would like to thank Univ.-Prof. DI Dr. Helmut Clemens, head of the Department of Physical Metallurgy and Materials Testing, for the possibility to carry out this thesis at his department.

My sincerest gratitude is due to Univ.-Prof. DI Dr. Christian Mitterer, head of the Chair of Functional Materials and Materials Systems, for his supervision, for all the helpful suggestions, for his patience and for everything I was able to learn from him.

Furthermore, I am very grateful to DI Thomas Weirather for investing so much time and finally “taming” Conny.

I would also like to express my gratitude to all the people from the thin film group for the pleasurable working atmosphere and for having such a great time. Especially, I am deeply grateful to DI Dr. Jörg Paulitsch. Thank you for your great support and advice, for being a good friend and for all the nice and funny coffee breaks!

I would also like to express my thankfulness to all those friends, who remain unnamed, but have also made their contribution to my achievements.

Danksagung

Ein ganz besonderes Dankeschön gilt meinen Eltern, Barbara und Willibald, für ihre Unterstützung während meines ganzen Lebens und insbesondere während meiner Studienzeit. Das Gleiche gilt für meinen Bruder Christian, dem ich außerdem für seine aufrichtige und loyale Freundschaft danken möchte.

Weiters möchte ich mich bei meinem Freund Dominik bedanken, der mich vor allem während der Diplomarbeit äußerst liebevoll und geduldig unterstützt und motiviert hat und mir immer Zuversicht gegeben hat, wenn mir alles zu viel wurde. Abschließend möchte ich noch sagen, dass ich sehr dankbar dafür bin, Menschen wie euch in meinem Leben zu haben und zu wissen, dass ihr immer für mich da seid.

Contents

Contents I
Table of figures III
List of tables IV
1 Introduction 1
2 Sputter Deposition 2
2.1 Thin film growth 5
2.1.1 Nucleation 5
2.1.2 Microstructure 6
3 Mechanical and Tribolgical Properties 9
3.1 Mechanical Properties 9
3.1.1 Hardness and Young's Modulus 9
3.1.2 Residual Stresses 9
3.2 Tribological Properties 10
3.2.1 Friction 10
3.2.2 Wear 11
4 Al-containing transition metal nitrides 13
5 Experimental Details 15
5.1 Film Deposition 15
5.1.1 Deposition System 15
5.1.2 Deposition Procedure 16
5.2 Film Characterization 17
5.2.1 Chemical Composition 17
5.2.2 Film Thickness 17
5.2.3 Film Adhesion 17
5.2.4 Microstructure 18
5.2.5 Film Stress 19
5.2.6 Hardness and Young's Modulus 20

5.2.7 Tribological Properties 21

6 Results 22

6.1 Film Thickness 22

6.2 Film Adhesion 22

6.3 Chemical Composition 23

6.4 Microstructure and Morphology 23

6.5 Residual Stress 25

6.6 Hardness and Young's Modulus 26

6.7 Tribological Properties 26

7 Discussion 33

7.1 Deposition – structure – property relations 33

7.2 Comparison between sputtered and arc evaporated CrAlN films 37

8 Summary and Conclusions 38

References 40

Table of figures

Fig. 2.1: Three types of PVD processes. 2
Fig. 2.2: Representation of a balanced and an unbalanced magnetron sputtering cathode. 4
Fig. 2.3: Three modes of thin film growth processes 5
Fig. 2.4: Structure zone model by Thornton and Messier *et al*. 7
Fig. 3.1: Input and output parameters of a tribosystem 10
Fig. 3.2: Basic mechanism of friction: adhesion, plowing and asperity deformation. 11
Fig. 3.3: Basic wear mechanisms: adhesive, abrasive, fatigue and chemical wear. 12
Fig. 4.1: Isothermal cut at 1000°C of the ternary phase diagrams Ti-Al-N and CrAlN 13
Fig. 4.2: Structural development of $TM_{1-x}Al_xN$ with increasing Al-content 14
Fig. 5.1: Picture of the arrangement of the Cr and Al targets and the TiAl targets 15
Fig. 5.2: The substrate carousel of the sputtering plant and the specimen holders. 16
Fig. 5.3: Schematic of the ball crater technique 17
Fig. 5.4: Different classes of film adhesion. 18
Fig. 5.5: Schematics of the stress measurement via two laser beams. 19
Fig. 5.6: Load-displacement curve resulting from a nanoindentation measurement. 20
Fig. 6.1: Film thickness of the Bilayer and the Multilayer. 22
Fig. 6.2: Me/(Al+Cr) atomic-ratio of the Bilayer and the Multilayer 23
Fig. 6.3: Gracing incidence XRD patterns of the Bilayer and the Multilayer. 24
Fig. 6.4: SEM fracture cross-section of theBilayer and the Multilayer 25
Fig. 6.5: Residual stresses of the Bilayer and Multilayer 26
Fig. 6.6: Hardness and Young's modulusfor the Bilayer and the Multilayer 26
Fig. 6.7: Friction coefficient and wear track profiles of the Bilayer 29
Fig. 6.8: Friction coefficient and wear track of the Multilayer 31
Fig. 6.9: Optical micrograph of the wear track 31
Fig. 6.10: Wear coefficients at different temperatures for the Bilayer and the Multilayer. 32
Fig. 7.1: Arrangement of the SNUN samples and the segmented Cr and Al targets. 33
Fig. 7.2: Sputtering yield of Cr with Ar^+ and Al with Ar^+. 35

List of tables

Table 5.1: Operating parameters used for XRD measurements. 18
Table 6.1: Film adhesion classes. 22
Table 7.1: Comparison of properties of arc-evaporated and sputtered CrAlN films. 37

1 Introduction

For many different applications, such as tools and dies for machining, forming and casting, special material properties are required [1]. They often can not be achieved with the bulk material solely; thus, deposition of thin films is required to modify and increase the functionality of the bulk surface. A widely used method for depositing such thin, wear protective films is the physical vapor deposition (PVD) technique. This technique allows the deposition of hard coatings with a wide range of chemical compositions and structures, as well as at different temperatures. If the properties of a single-layer thin film are not sufficient for a certain application, there is also the possibility to vary the film architecture by the means of gradients or multilayer structures [2].

Hard films like TiAlN and CrAlN are very successfully used for cutting applications, due to their excellent oxidation and wear resistance, friction behavior and mechanical properties. These properties are strongly depending on the chemical composition of such coatings, as e.g. an increase in Al-content enhances the film properties until reaching a critical Al-value at which a transition from the metastable cubic to the undesired stable hexagonal wurzite phase occurs [3-5]. To study this structure-property dependence, over a broad compositional range, numerous deposition runs with several conventional targets of fixed compositions are required. In order to reduce the expenditure of time and subsequently saving costs, segmented triangle-like targets were developed for an industrial-scale magnetron sputtering system. Such targets, as used in the present work, allow a broad variation in the chemical composition at high resolution in one single deposition run.

Two different film architectures were deposited to investigate the influence of the Al-content onto film properties. Those were, the TiAlN-CrAlN Bilayer and Multilayer, using powder metallurgically synthesized homogenous TiAl sputter targets with an Al-content of 60 at.% and the segmented, triangle-like Cr and Al sputter targets. For both film architectures, a TiAlN base layer was deposited to provide a constant film adhesion to the cemented carbide substrates. The deposition of a bilayered CrAlN and TiAlN as well as multilayered CrAlN/TiAlN films was achieved by successively powering the TiAl and CrAl cathodes, or by powering all cathodes at the same time, respectively, at multifold substrate rotation. The influence of changing Al-content was investigated by studying the microstructure as well as the mechanical and tribological properties of the films.

2 Sputter Deposition

Sputter deposition is an important sub-discipline of physical vapor deposition (PVD) techniques. PVD allows the deposition of nearly every kind of material – metals, compounds, alloys as well as some organic materials - on a broad variety of substrate materials. The main steps in PVD processes are (i) the creation of the vapor phase, (ii) the transfer of the vapor from the source to the substrate and (iii) the condensation of vapor and nucleation and growth onto the substrate [6].

The transfer into the vapor phase can be achieved by three different types, which can also be used for a classification of PVD processes (Fig. 2.1):

- Evaporation (coating material is heated by e.g. radiation, electron beam, arc discharge)
- Sputtering (bombardment of the coating material by ionized gas)
- Ion Plating (combination of sputtering and evaporation, substrate is bombarded by high-energy gas ions) [1, 6].

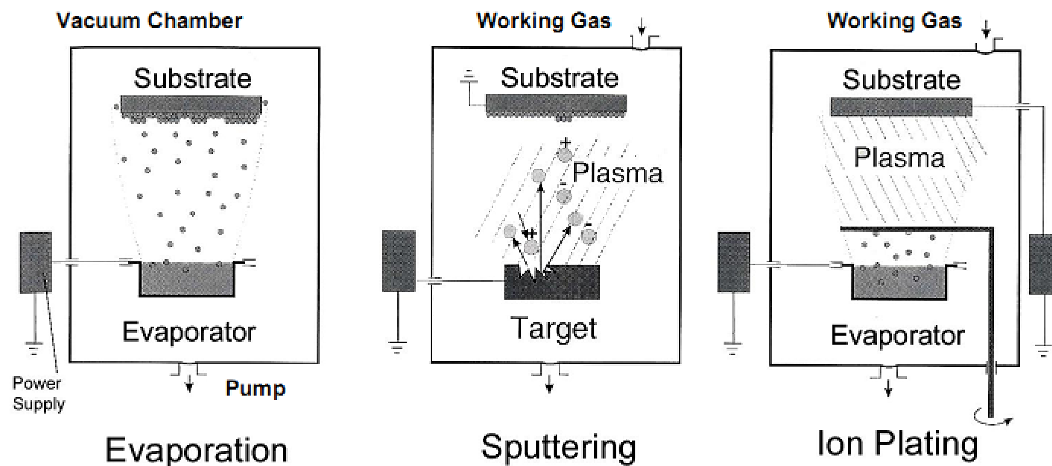

Fig. 2.1: Three types of PVD processes [7].

For this diploma thesis all films are deposited by sputter deposition; thus this method will be described in detail.

Sputter deposition is carried out in a vacuum chamber. Here, the solid deposition material (the so-called target) and the material to be coated (substrate) are in the simplest arrangement (the so-called diode sputtering) positioned face to face and a working gas, usually argon is introduced. The transformation of the target into the vapor state occurs by bombardment with energetic ions (e.g. Ar^+), provided by a glow discharge (plasma). The ions are accelerated by an electric field towards the target and transfer their energy and momentum to the surface atoms of the target material. As a result some atoms receive an energy which is higher than

the surface binding energy and leave the target. Almost all ejected particles are neutral. For the process development it is important to know the "resistance" of the target against ion bombardment. This "resistance" can be described by the sputter yield Y, which is defined as the ratio between the number of ejected atoms and the number of incident ions [1, 7 – 12].

In order to deposit e.g. some nitride- or oxide compounds a reactive gas is added to the working gas. The compounds can be formed by: (i) the formation on the target surface and sputtering of these molecules, (ii) the formation in the gas phase and subsequent deposition and (iii) the adsorption of reactive gas on the substrate, followed by reaction with the target atoms. A benefit of the reactive sputtering process is, that with variation of the partial pressure of the reactive gas, the stoichiometry of the deposited film can be adjusted [11, 12].

To achieve higher deposition rates compared to simple diode glow discharge systems, magnetron sputtering is used. Here, permanent magnets are placed behind the target, generating a magnetic field B which superimposes the electric field E of the glow discharge. As a result of the $E \times B$ drift, the electrons follow a closed circular path along the magnetic field lines. Due to their lower mass, electrons are more influenced by B than ions. As a result, only the electrons are trapped near the target and forming a circular current, which is also known as racetrack. Hence, there is a high concentration of electrons that leads to a higher ion density. This increases the ion bombardment of the target, leads to higher sputtering rates and consequently higher deposition rates at the substrate [10, 13, 14].

In Fig. 2.4, a balanced and an unbalanced magnetron sputtering cathode is shown. In the case of a balanced magnetron, the strength of the inner and outer magnets is equal and most of the magnetic field lines will loop between the inner and the outer magnets. If either the outer or the inner magnets are made stronger than the others, the magnetron is called unbalanced. In this case most field lines from the stronger magnets will radiate away and guide more ions to the substrate [13].

A problem in reactive magnetron sputtering is the formation of an insulating compound layer consisting of the reactive gas and the target material on the target surface (the so-called target poisoning). Poisoning leads to reduced sputtering rate and efficiency. Due to the compound formation a charge is built up and then, after the charge reaches the breakdown voltage, a discharge during sputtering occurs, also called "arcing" [1, 10].

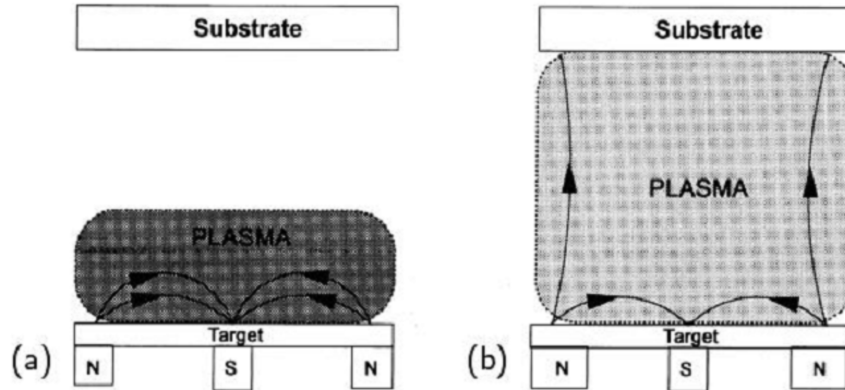

Fig. 2.2: Schematic representation of a balanced (a) and an unbalanced (b) magnetron sputtering cathode [15].

To prevent arcing during reactive magnetron sputtering, the applied voltage can be pulsed in either unipolar or bipolar mode. By applying a unipolar pulsed voltage, the voltage varies between ground and normal negative operation voltage. For a bipolar pulsed voltage, the polarity of the target alternates from negative to positive. A bipolar pulse with equal voltage values in positive and negative direction is called symmetric. The ratio between the negative pulse time and the period (equal frequency^{-1}) is called duty cycle. During the negative pulse, ions are attracted to the target and sputtering occurs, while during the positive pulse electrons are attracted to the target, reducing the charge build-up and thus avoid arcing.

In case of pulsed dual magnetron sputtering, two magnetrons are connected to the same pulse supply. Here, one leg of the output of the power supply is wired to one target, and the other leg to the other target. If one target is negative with respect to the plasma, the other one is positive and acts as the anode. In the next half cycle, the voltages are reversed and the target that was first the cathode, and is sputtered, is now the anode. Due to this change in polarity, a discharging effect at the target takes place [13, 15, 16].

There is also the possibility to apply a negative direct-current (DC) or radio-frequency (RF) bias voltage to the substrate. As a consequence, during thin film growth, the film is bombarded with charged particles of the sputter gas. The impinging particles cause a local heating of the substrate, also called atomic scale heating. Due to this heating atomic motion, like diffusion and stress annealing, and higher ad-atom mobility occurs and the film structure can be influenced positively. Furthermore, the bombardment of the growing film leads to "atomic peening". There, surface atoms are hit and fill up voids and thus, a densification of the film occurs [9, 10, 12].

A further possibility is the pulsed bias sputtering. If the substrate is on a negative potential, the growing film is bombarded by positive energetic ions. But if the substrate is on a positive

potential, electron treatment of the growing film occurs. Similar to pulsed DC sputtering a classification between unipolar and bipolar pulsed voltages can be made. With pulsed bias sputtering it is possible to deposit with higher bias voltages, at lower temperatures and to achieve dense films [17-19].

2.1 Thin film growth

2.1.1 Nucleation

When sputtered particles collide with the substrate, they are either reflected or if they transfer enough energy to the substrate lattice, they become loosely bonded [12]. Those so-called ad-atoms diffuse over the substrate surface, where they interact among themselves and may form bigger clusters or are desorbed. If the clusters become thermodynamically stable, they are called nuclei and the formation of the clusters is called nucleation. The nucleation density, which is defined as the number of nuclei per unit area, and the nucleus size depend on the energy of the impinging species, the rate of impingement, the activation energies of adsorption, desorption and diffusion, the temperature and the chemical nature of the substrate [20]

Enlargement of the nuclei occurs similar to nucleation, by direct impingement of incident particles or surface diffusion of the ad-atoms. This enlargement is termed growth. There are three film growing modes, depending on the thermodynamic parameters of the deposit and substrate surface: (i) island growth (Vollmer-Weber mode), (ii) layer-by-layer growth (Frank-van der Merwe mode) and (iii) layer plus island growth (Stranski-Krastanov mode) (see Fig. 2.5) [21].

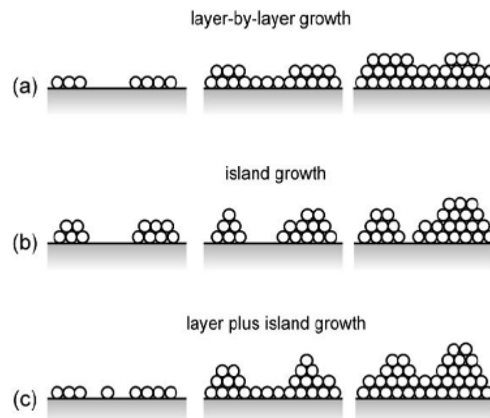

Fig. 2.3: Three modes of thin film growth processes: (a) Frank-van der Merwe or layer-by-layer growth, (b) Vollmer-Weber or island growth and (c) Stranski-Krastanov or layer plus island growth [22].

In the layer-by-layer mode, the interaction of the substrate atoms and the ad-atoms is stronger than that between the ad-atoms, whereas in the island growth mode the opposite happens. In the layer plus island mode, after the formation of one or several monolayers, island formation occurs [21].

2.1.2 Microstructure

The parameters applied during the PVD process influence the microstructure and subsequently the properties of thin films [19]. If the film formation is understood, there is the possibility to manipulate and control the microstructure and furthermore develop a material for specific applications. As a consequence, structure zone models (SZM) have been developed [24].

The first SZM was published by Movchan und Demchisin [25]. They observed that the microstructure of thick evaporated Ti, Ni, W, ZrO and Al_2O_3 films could be represented by a single SZM, where the film thickness is plotted versus the homologous temperature T_s/T_m (T_s is the substrate temperature and T_m is the film material melting point). They found three zones:

In *Zone 1* ($T_s/T_m<0.3$) ad-atom mobility is not high enough to compensate shadowing effects. A fine fiber texture will be developed, whereby the fibers grow out of a relative minor number of nuclei. The structure is rather homogenous along the coating thickness and porous.

The *Zone 2* ($0.3<T_s/T_m<0.5$) is characterized by grain boundary migration, which leads subsequently to grain boundaries that are nearly perpendicular to the film plane. The film shows a homogenous structure in growth direction and is composed of columnar crystals with similar orientation. With increasing T_s, the diameter of the columns increases, while the porosity decreases.

When the homologous temperature becomes higher than 0.5, crystal growth will be blocked periodically. The structure in this *Zone 3* is characterized by equiaxed three dimensional grains. Bulk diffusion is decisive and a recrystallized and dense structure occurs [12, 24 – 28].

Thornton enhanced this SZM for sputter deposited thin films and included the dependence on the inert sputtering gas pressure. This led to a fourth zone in Thornton’s model (Fig.2.6 (a)), the so called transition zone (*Zone T*), which is located between *Zone 1* and *Zone 2* [12].

In *Zone T*, the surface diffusion partially compensates the shadowing effects. A fibrous and denser structure than in *Zone* 1 is developed by competitive growth of differently oriented neighboring crystals. This zone belongs to the temperature interval $0.2 < T_s/T_m < 0.4$ and exhibits an inhomogeneous structure along the film thickness.

Thornton observed that with increasing inert gas pressure also the transition temperatures increase [8]. Because of the increasing pressure, the mean free path for collisions between the inert gas atoms and the sputtered atoms decreases. Due to this collisional scattering the energy of the deposition flux is reduced [14].

Messier *et al*. included the bias potential in their SZM, as shown in Fig. 2.6 (b) [23]. With increasing the bias voltage also the ion flux onto the substrate surface increases [29]. The impinging ions transmit their energy to the ad-atoms, leading to higher mobility of them. As a result at a given T_s/T_m a denser structure with crystallites of a larger diameter occurs and the transition between zones shift to lower T_s/T_m values [12].

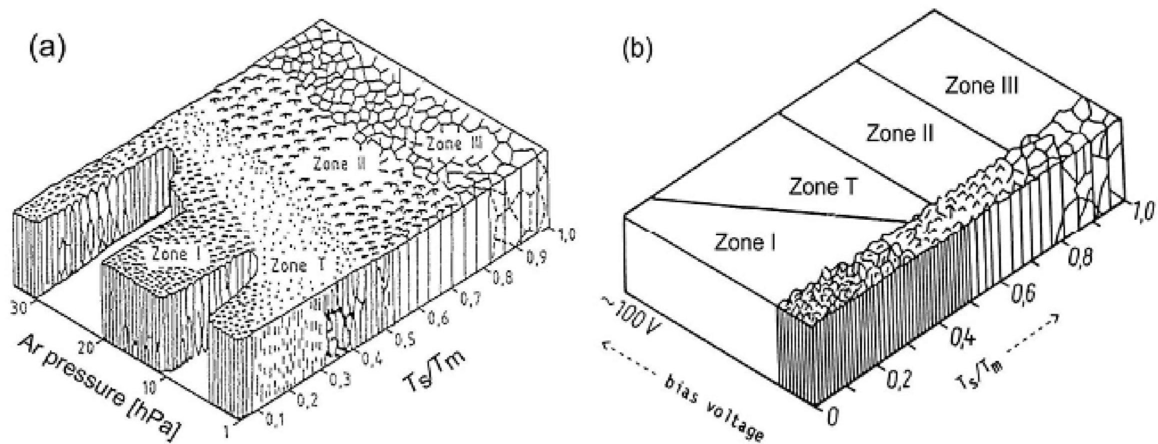

Fig. 2.4: Structure zone model by (a) Thornton [26] and (b) Messier *et al*. [23]

Barna *et al.* developed the so called real SZM that represents the temperature dependent structures at different concentrations of impurities [27].

For a *Zone 2* structure this means that at low impurity concentration level the grain growth in the coalescence stage is not restricted notably. But due to the decreased mobility of the grain boundaries the further grain growth will be limited. As a result the columns are narrower compared to those of *Zone 2* in the basic model. For a medium concentration the grain growth will already be limited in the coalescence stage. A *Zone T* structure and competitive growth texture develops. At a high concentration level, crystal growth is blocked periodically

and a structure like that in *Zone 3* with three dimensional equiaxial randomly oriented, small grains occurs [27].

3 Mechanical and Tribolgical Properties

3.1 Mechanical Properties

3.1.1 Hardness and Young's Modulus

In material science hardness, *H,* can be defined as the resistance of a material against plastic deformation caused by a harder material [30]. *H* can be obtained by pressing an indenter into the surface and evaluating the residual imprint. Then *H* is given by the ratio between the applied load *P* and the residual projected area *A* [30]:

$$H = \frac{P}{A} \tag{3.1}$$

The hardness of thin films depends on the chemical composition, the morphology and the atomic binding energy. Furthermore, measurement conditions and the hardness of the substrate material possibly influence the measurement results. Therefore, to ensure that only the hardness of the film will be measured, the indentation depth should be less then 10% of the film thickness [31].Thin film hardness increases with increasing binding energy per molar volume, as well as for thin films that shows residual compressive stresses. Cavities on grain boundaries and pores, however, decrease the hardness of the film [28].

The Young's Modulus *E,* is a measure for the elasticity, or stiffness of a material and it is related to the binding energy of atoms [32]. The higher the binding energy the higher are the required forces to separate the atoms, and cause the material to stretch elastically. Thus the higher is *E*. Furthermore, materials with high melting points show high *E* values. A problem in measuring *E* is that "the elastic modulus so measured, no matter how small the penetration depth, is a combined modulus of the film and substrate system", due to the huge extension of the elastic stress field under the indenter [33].

3.1.2 Residual Stresses

Residual stresses in thin films produced by PVD may lead to defect formation and delaminations at the film substrate interface. Thus, it is necessary to know about the origin of stresses and to control their magnitude, σ_{tot}. There are two parts that contribute to σ_{tot}: (i) the intrinsic stresses σ_i and (ii) the thermally induced stress σ_{th}:

$$\sigma_{tot} = \sigma_i + \sigma_{th} \tag{3.4}$$

Intrinsic stresses are related to the microstructure of thin films and are generated during nucleation and thin film growth. They occur e.g. because there are usually some defects in the film structure. Thermal stresses are generated during cooling down the sample after deposition at elevated temperatures. They are a result of different coefficients of thermal expansion of the film and substrate.

The stresses lead either to compression or tension, so that the film tries to contract or expand parallel to the surface and cause the substrate-film composite to bend [10, 27, 34].

3.2 Tribological Properties

Tribology is the science and technology of contacting surfaces in relative motion and deals with the topics of friction, wear and lubrication. The coefficient of friction and other tribological properties are related to a so called tribosystem. That is a system of materials, lubricants and other influence parameters as shown in Fig. 3.3 [35, 36].

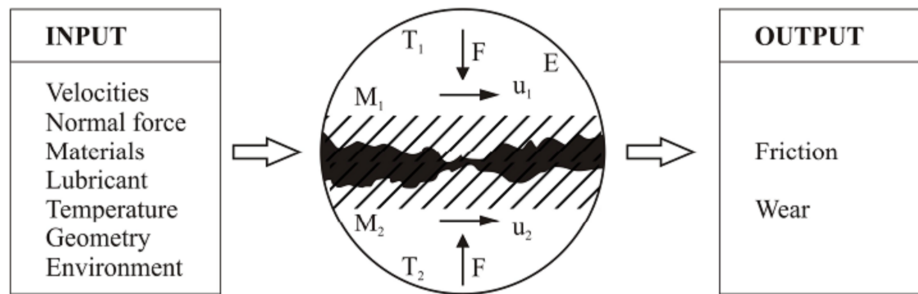

Fig. 3.1: Input and output parameters of a tribosystem [36].

3.2.1 Friction

Friction is the resistance to motion of two contacting bodies, where one of the bodies is moved tangentially with respect to the surface of the other one. It can also be said that friction is the dissipation of energy between sliding bodies [35, 36].

The ratio between the frictional force, F_R, and the normal load, F_N is known as the coefficient of friction, μ

$$\mu = \frac{F_R}{F_N} \quad . \tag{3.7}$$

Depending on the type of relative motion between two contacting bodies, a distinction has to be made between sliding and rolling [35].For the present work only sliding is important and hence only sliding friction is discussed in more detail.

Bowden and Tabor (1950) developed a concept, which explains the mechanism of sliding friction by the adhesion between surface asperities. They also included the plowing effect. Suh and Sin [38] presented a concept, wherein a distinction in three basic mechanisms of friction was made (see Fig. 3.4). Here friction is caused by: (i) adhesion, (ii) plowing and (iii) asperity deformation.

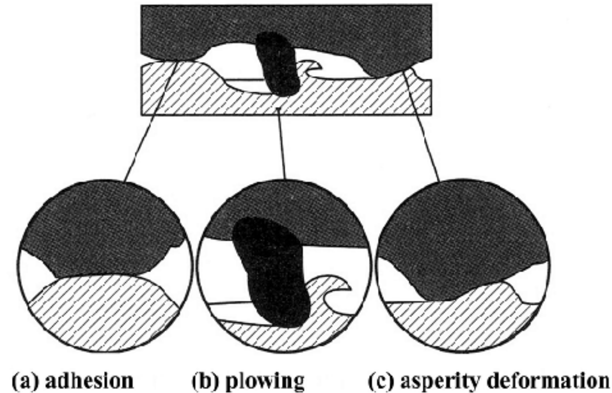

Fig. 3.2: Schematic of the three basic mechanism of friction: (a) adhesion, (b) plowing and (c) asperity deformation [36].

If there are two bodies in contact, there are areas of real contact at the surface, which are called asperity junctions. Between the asperities attractive forces are working and they adhere, which means they weld together. These junctions break if the two bodies are in relative motion and slide over each other. Thus, a resistance to motion due to *adhesion* appears. Furthermore, hard particles or asperities that penetrate into a softer material and build up furrows by plastic flow, create a resistance to motion. This mechanism is called *plowing*. Due to elastic and plastic *deformation of asperities* a physical work is performed. This contributes as well to a resistance against motion [35, 36].

3.2.2 Wear

Wear is the removal of material from a surface when two contacting bodies are moving over each other. The way this removal occurs can be described by different wear mechanisms, which are (i) adhesive, (ii) abrasive, (iii) fatigue and (iv) chemical wear, as shown in Fig. (3.5).

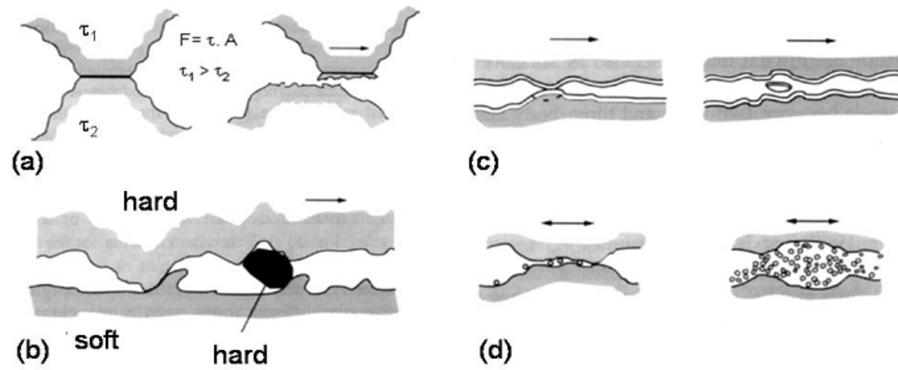

Fig. 3.3: Schematic of the basic wear mechanisms: (a) adhesive, (b) abrasive, (c) fatigue and (d) chemical wear [35].

Adhesive wear takes place if two bodies are in contact and the asperities of one surface adhere strongly to the asperities of the other one. Due to relative motion of the surfaces, softer asperities are separated and material is removed. If one of the contacting surfaces is harder than the other or if there are hard particles introduced into the contact, the harder asperities are pressed into the softer surface. This leads to plastic flow of the softer material and subsequently to removal of the softer material. This mechanism is called *abrasive wear* and as a result grooves or scratches remain on the surface. Wear caused by hard surface asperities it is specified as two-body abrasive wear, while wear caused by hard particles in the contact is called three-body abrasive wear. If repeated loading and unloading cycles of the surface at stress levels that the surface can sustain once, but not several times, happens, *fatigue wear* takes place. These loading and unloading cycles lead to cracks in the surface or subsurface and this may lead to breakup of surface and liberation of surface material. Introduced by mechanical contact mechanisms combined with the influence of the environment, detrimental chemical reactions take place, called *chemical wear*. The most common wear process here is oxidational wear, where a film of oxides forms on the surfaces and acts as a protecting layer against friction and wear. In combination with rubbing, removal of material occurs. The layer is not longer protecting and the surface can be subject to wear [35 – 37].

4 Al-containing transition metal nitrides

The deposited and analyzed films in the present work are titanium aluminum nitride (TiAlN) and chromium aluminum nitride (CrAlN), thus they are described in detail. Transition metal nitrides (TMN) films, like TiN and CrN are widely used as wear reduction and protective films on tools and components for forming, casting and machining applications. For TiN there are some drawbacks, like hardness, friction, oxidation resistance and adhesion, which limit its application compared to CrN. By the addition of Al to TiN and CrN wear and oxidation resistance are significally improved [39 – 44].

The binary nitrides TiN and AlN as well as CrN and AlN show very low solubility for each other in thermodynamic equilibrium. This can be seen in Fig. 4.1 by an isothermal section of the ternary phase diagrams Ti-Al-N and Cr-Al-N at 1000°C [40].

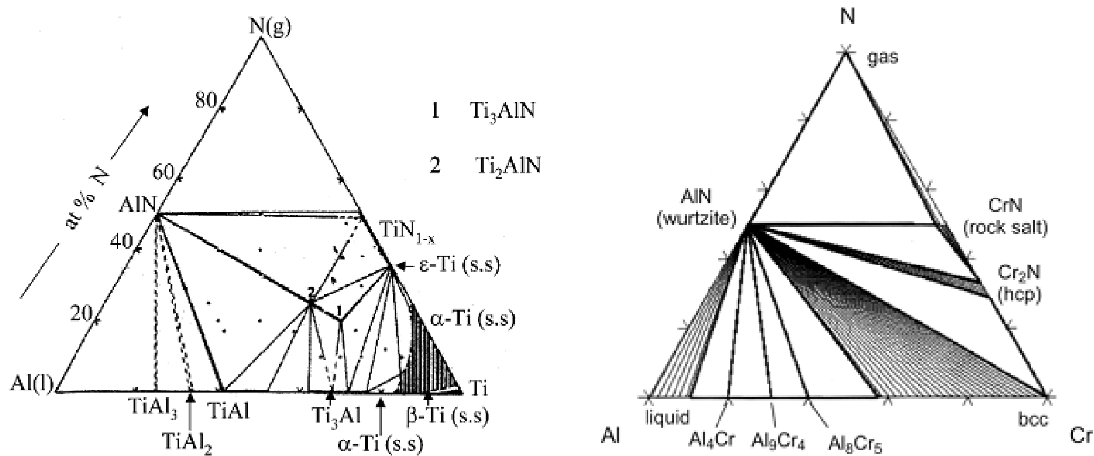

Fig. 4.1: Isothermal cut at 1000°C of the ternary phase diagrams Ti-Al-N and CrAlN [1, 40].

The growth of PVD thin films is based on free atoms and particles with momentum as well as energy transfer. Thus, PVD is a non-equilibrium process and it is possible to deposit metastable solid solutions, and there are no thermodynamic limits in the composition range of ternary films [43, 44].

As shown in Fig. 4.2, the crystal structure for the pseudo-binary Al-containing TMN changes from the cubic B1 (NaCl) structure to the hexagonal B4 (wurzite) structure with increasing Al-concentration x. If a critical Al-content x_{crit} is reached, transformation from B1 to B4 occurs. However, initially the simultaneous crystallization of the B1 and B4 phases is obtained in the transition zone, before at higher x only the B4 structure exists The transition zone for the TiAlN system is located at x values of about 0.6 to 0.7 and for CrAlN at about 0.7-0.77 [3, 39 – 45].

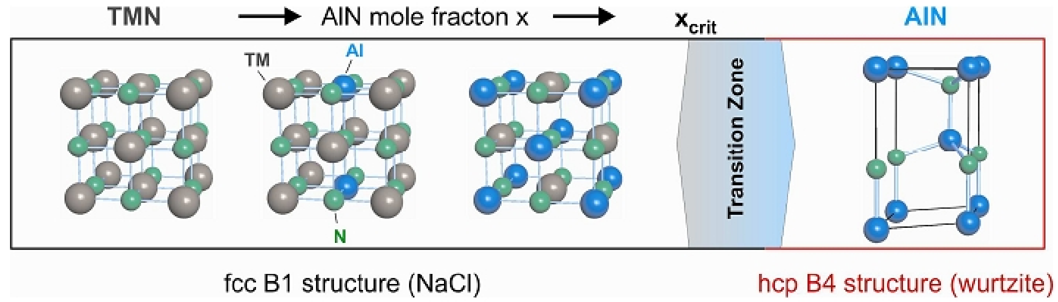

Fig. 4.2: Structural development of $TM_{1-x}Al_xN$ with increasing Al-content [46].

The TM atoms are substituted by the smaller sized Al atoms and thus the lattice parameter decreases with increasing x. The lattice parameter for pure TiN is 4.2448 Å and for CrN 4.174 Å, whereas for B1 type AlN it is 4.1462 Å [5, 40, 41].

In general, mechanical properties improve with increasing Al content until x_{crit} is reached. For example, the hardness and the Young's modulus increase until x_{crit} is reached. Accordingly both, hardness and Young's modulus decrease rapidly, as a result of formation of the hexagonal B4 structure. Zhou *et al*. [41] explained the increase of hardness by the fact that the interatomic distance decreases. The residual stress shows the same behaviour until x_{crit} is reached. This can be explained by the dissolution of Al atoms, which induces strain in the film. Furthermore the residual stress, which is generally compressive, decreases rapidly when the Al-content exceeds x_{crit}. Due to the smaller lattice parameter of AlN, the volume shrinks and tensile stresses are generated. Moreover, the wear resistance as well as the coefficient of friction increase with increasing Al-content. Additionally, the oxidation resistance is enhanced. This is because a dense Al_2O_3 surface layer is formed, which acts as a diffusion barrier, and thus diffusion wear is reduced. CrAlN exhibits higher oxidation resistance than TiAlN, because both Cr and Al could form protective oxides [3, 5, 39 – 41, 45]. At elevated temperatures, the metastable cubic-TiAlN solid solution can spinodal decompose into TiN and AlN. In the early stages, hardness increases, due to formation of coherent AlN and TiN domains which hinder dislocation movement. A further increase in annealing temperatures results in a decrease in hardness due to the precipitation of an incoherent hexagonal AlN equilibrium phase [47].

5 Experimental Details

5.1 Film Deposition

5.1.1 Deposition System

For the present work, all films have been deposited with an industrial-scale sputtering device of the type CemeCon CC800®/9MLT by reactive unbalanced magnetron sputtering. The device is equipped with four bipolar pulsed magnetrons of the size 500x80 mm. The TiAl targets of the size 500x88 mm are fixed on one cathode pair. On the other pair of cathodes the Cr and Al targets, with triangular shape and a size of 200x88 mm are fixed (see Fig. 5.1). All targets used were powder metallurgical targets produced by PLANSEE Composite Materials in Lechbruck, Germany. The TiAl targets contained 60 at.% Al and 40 at.% Ti.

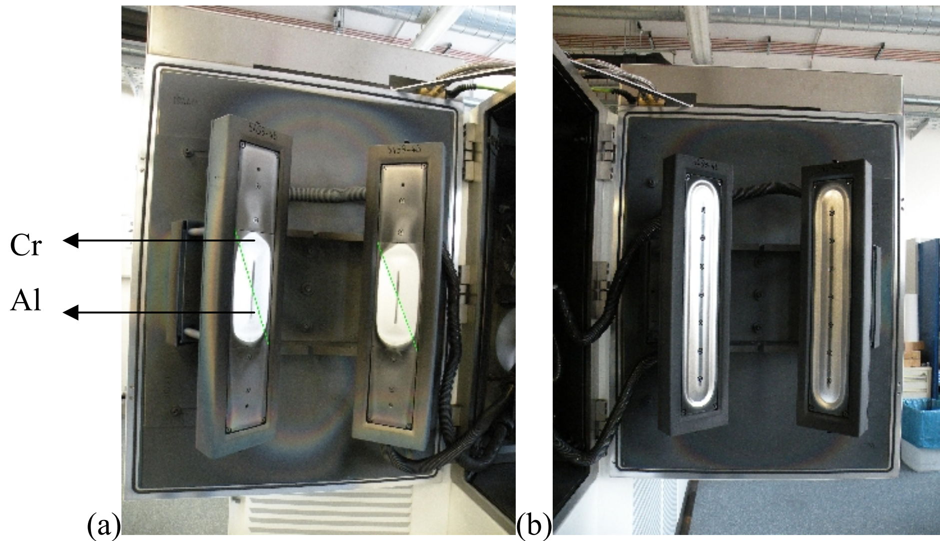

Fig. 5.1: Picture of the arrangement of the Cr and Al targets (a) and the TiAl targets (b).

The substrates were mounted on the substrate carousel, which consists of 6 sample holders. Here, the substrate carousel as well as each of the 6 sample holders rotates. Four different types of substrates were mounted as shown in Fig. 5.2: i) Si (100) samples, (ii) cemented carbide inserts with SNUN geometry, (ii) cemented carbide disks, and (iv) cemented carbide cutting inserts of type SEKW. The cemented carbide samples of type S26T consist of 9.5 wt.% Co, 8.6 wt.% TiC, 10.8 wt.% TaC, 1.2 wt.% NbC and 69.9 wt.% WC. 28 Si pieces were attached and numbered consecutively, starting with 1 at the top of the specimen holder up to 28 on the lowest position. For the SEKW and the SNUN samples, the designation was

made in the same manner, but the numbering is only from 1 to 15. Furthermore, 5 cemented carbide disks were mounted and numbered from 1 to 5.

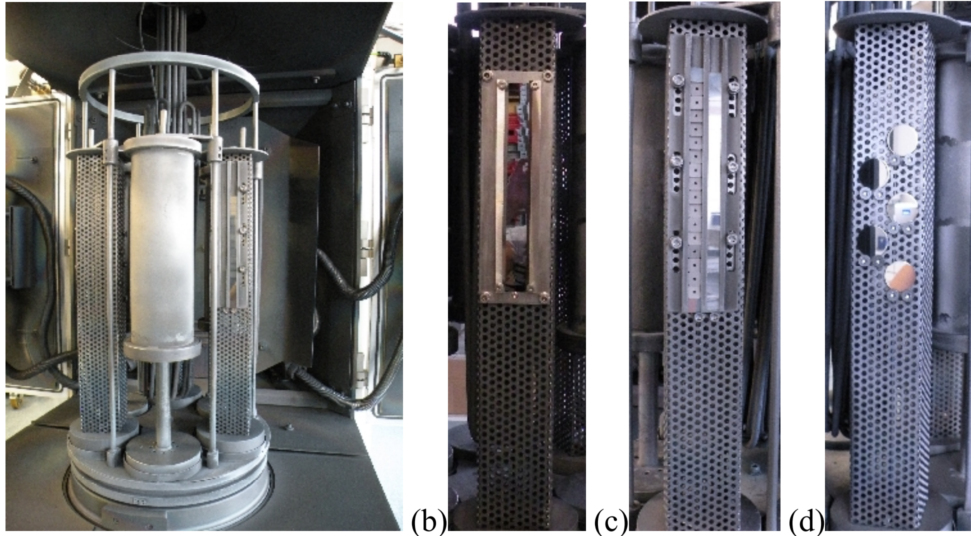

Fig. 5.2: The substrate carousel of the sputtering plant (a) and the specimen holder for: (b) the Si samples, (c) the SNUN and SEKW samples and (d) the cemented carbide disks.

5.1.2 Deposition Procedure

The substrates were first ultrasonically cleaned in acetone and ethanol for 10 minutes and then mounted on the substrate carousel of the sputtering plant. With the CemeCon CC800®/9MLT the deposition processes recipes can be programmed and run automatically. Similar for both deposition processes, the chamber is first evacuated to a base pressure of ≤ 4 mPa. Then, the substrates were cleaned by a heating step followed by an etching step. There, the substrate carousel acts as the cathode and the substrates are bombarded by Ar^{+} ions from the ignited plasma. During the next step booster etching takes place.

After cleaning the substrates, the actual deposition process is started. As for both film systems a TiAlN base layer is deposited, the deposition parameters for it were equal. There, the TiAl cathodes were dual pulsed with a frequency of 20 kHz and a duty cycle of 50 %. The cathode power for both was set to 5 kW. Furthermore, a unipolar pulsed bias voltage of -60 V at a pulse frequency of 350 kHz and a reversal time of 1 µs was applied. The deposition temperature of 520°C and the total pressure of 650 mPa were held constant. After the deposition of the TiAlN layer, the processes for the Bilayer and the Multilayer differ. For the Bilayer only the CrAl equipped cathodes were now dual pulsed with a frequency of 20 kHz and a duty cycle of 50 %, while in case of the Multilayer both, the CrAl and TiAl cathodes, were operated at the same time. The CrAl cathode power was set to 1.1 kW. The total deposition time for the Bilayer and the Multilayer was 8.5 and 6.75 h, respectively.

5.2 Film Characterization

5.2.1 Chemical Composition

For determining the chemical composition of the films, an energy-dispersive x-ray spectroscopy (EDX) utilizing an Oxford Instrument INCA system in a Zeiss EVO 50 scanning electron microscope (SEM) was used. The acceleration voltage was set to 7 kV and the implemented standards of the SEM were used. The chemical composition of the Bilayer was measured on every SNUN and of the Multilayer on 4 SNUN samples.

5.2.2 Film Thickness

The film thickness t_f was measured on the Si samples by the ball crater technique, schematically shown in Fig. 5.1.

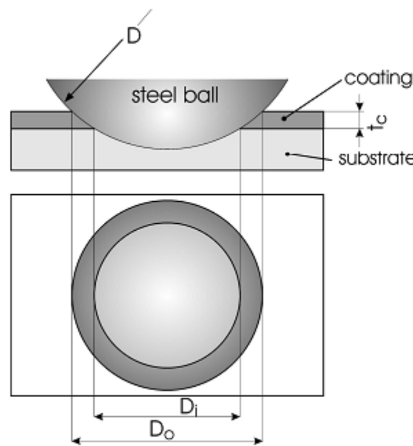

Fig. 5.3: Schematic of the ball crater technique [48].

There a steel ball, which is covered with a diamond suspension, is used to grind a spherical calotte in the coating by rotational movement. The inner (D_i) and the outer (D_o) diameters are measured by an optical Reichert-Jung microscope of type Polyvar Met with an attached CCD camera and the analySIS® software of Soft Imaging System. The film thickness is derived according to:

$$t_f = \frac{D_o^2 - D_i^2}{4 \cdot D} , \qquad (5.1)$$

where D denotes the diameter of the steel ball [30].

5.2.3 Film Adhesion

A Rockwell C indentation test (DIN 50103 Part 1) was used to determine the film adhesion of the Bilayer and the Multilayer coatings on the cemented carbide disks. A Mitutoyo

Rockwell C hardness tester, type DT-10, was used for making indentations. Due to the indentation plastic deformation occurs, which leads to damage of the film around the indentation and thus, a crack network is formed. In case of insufficient adhesion, film delamination occurs. The indentations were then examined with an optical Reichert-Jung Polyvar Met microscope in order to compare the coating damage with the adhesion table after VDI guidline 3842 (Fig. 5.3) [49].

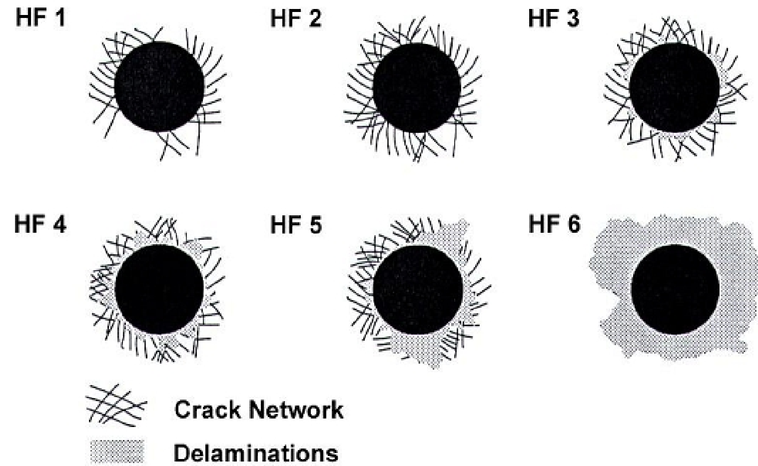

Fig. 5.4: Different classes of film adhesion, which are compared with the indentations of the Rockwell C indentation test [49].

5.2.4 Microstructure and Morphology

For characterization of the crystalline structure of the films, the x-ray diffraction (XRD) was used. All measurements in the present work were carried out with a Bruker D8 diffractometer in Bragg-Brentano and detector scan mode with grazing incidence of 2°. For all measurements, the same operating parameters were used (see Table 5.1). XRD measurements were conducted for the SNUN inserts and Si samples. The morphology and structure of the cross-sections of the films was investigated by SEM.

Table 5.1: Operating parameters used for XRD measurements.

Voltage [kV]	Tube current [mA]	Step time [s]	Step size [°]	Angle range [°]
40	30	1.2	0.02	25-85

5.2.5 Film Stress

Film stress was measured using the wafer curvature method. The schematics of the measurement setup are shown in Fig. 5.5.

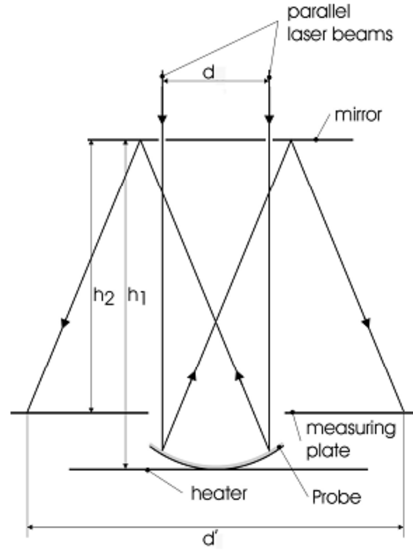

Fig. 5.5: Schematics of the stress measurement via two laser beams [50].

The surface of a coated silicon substrate is irradiated by two parallel laser beams with defined distance *d*. The beams are first reflected by the substrate surface and then by the mirror in the defined distance h_1. Finally, they hit the measuring plane in the distance h_2, where their distance between each other, d_1 can be measured.

By inserting this information in the following equation for the bending radius of the coated sample,

$$r = \frac{2 \cdot (h_1 + h_2) \cdot d}{d - d_1} \quad , \tag{5.2}$$

one can calculate the residual stresses by the modified Stoney equation:

$$\sigma = M \cdot \frac{t_s^2}{6 \cdot t_f} \cdot \left(\frac{1}{r} - \frac{1}{r_0} \right) \tag{5.3}$$

M and v_s are the biaxial modulus and the Poisson's ratio of the substrate, t_s and t_f are the thickness of the substrate and film, respectively, and r_0 is the bending radius of the substrate [50, 51].

Stress measurement was carried out on silicon samples for both, the Bilayer and the Multilayer.

5.2.6 Hardness and Young's Modulus

Hardness and Young's modulus were determined using a UMIS Nanoindenter (Ultra Micro Indentation System) from Fischer-Cripps Laboratories, equipped with a Berkovich indenter. The load *P* and the displacement *h* are measured continuously during a complete cycle of loading and unloading (see Fig. 5.6) [31].

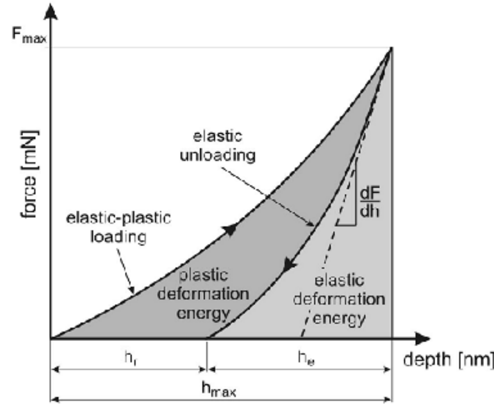

Fig. 5.6: Load-displacement curve resulting from a nanoindentation measurement [52].

In reality, the shape of the indenter is not ideal since the tip is always slightly rounded. To account for this, an area function in combination with the indentation depth is used to determine the real contact area. Moreover, the elastic properties of a material can be determined by nanoindentation.

By using the method of Oliver and Pharr [31], *E* can be derived from the slope of the initial portion of the unloading part of the load – displacement curve by

$$E_r = \frac{S\sqrt{\pi}}{2\sqrt{A}} , \tag{5.4}$$

where S is the initial unloading contact stiffness and defined as dP/dh, E_r the reduced Young's modulus and A the projected contact area under peak load. E_r can be calculated by

$$\frac{1}{E_r} = \frac{(1-\nu_f^2)}{E_f} + \frac{(1-E_i^2)}{E_i} , \tag{5.5}$$

where E_f and ν_f are the Young's modulus and Poisson's ratio for the film, and E_i and υ_i the same quantities for the indenter [31].

For determining H and E a plateau test was carried out with a maximum load of 15 mN and a minimal load of 5 mN with an increment of 0.4 mN on every SNUN sample.

5.2.7 Tribological Properties

The investigations of tribological properties were carried out by the ball-on-disk test [53] using a CSM High Temperature Tribometer. From each position on the substrate carousel, one cemented carbide disk was investigated at room temperature, one at 500°C and one at 700°C. A sliding distance *s* of 300 m, a normal load *F* of 5 N and a wear track radius *r* of 7 mm was chosen. The counterpart was an Al_2O_3 ball with a diameter of 6 mm. The acquisition rate was set to 10 Hz and the linear sliding speed to 10 cm/s.

The wear tracks were measured by white light interferometry (Veeco Wyko NT1000) in vertical scanning interferometry mode using the Wyko® Vision32 software. The negative wear volume *V* was determined by evaluation of a section of the wear track and the total wear volume V_{tot} was determined by the following equation:

$$V_{tot} = V \cdot \frac{(2 \cdot 3 \cdot \pi)}{l} \quad . \qquad (5.6)$$

Here, *r* is the radius of the wear track and *l* the length of the section for which the negative wear volume is determined.

Subsequently the wear coefficient *K* can be calculated as follows:

$$K = \frac{V_{tot}}{(F \cdot s)} \qquad (5.7)$$

Here, *F* is the normal load and *s* is the sliding distance [38].

6 Results

6.1 Film Thickness

The film thickness, measured on Si samples, versus the sample position of the Bi- and Multilayer is shown in Fig. 6.1. The mean film thickness is about 3.4 ± 0.2 μm for the Bilayer and 3.3 ± 0.2 μm for the Multilayer with slightly lower film thickness on both, the upper and lower positions. The TiAlN base layer is for both film architectures approximately 2 μm thick.

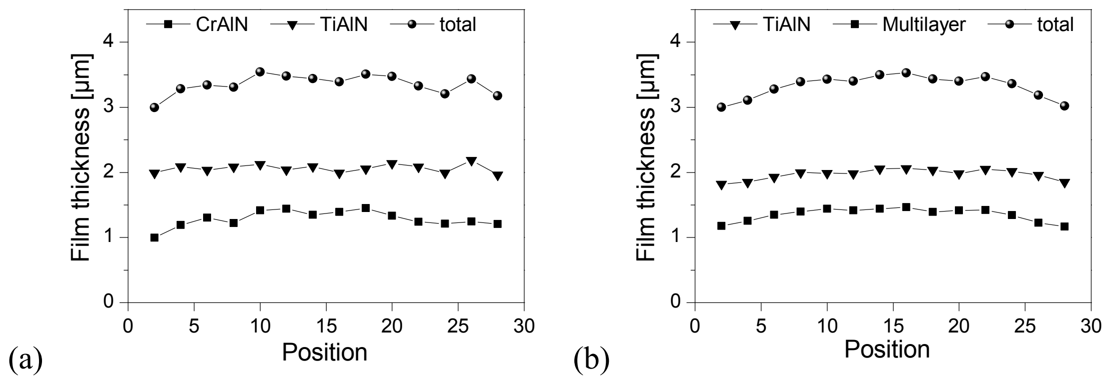

Fig. 6.1: Film thickness depending on the Si-sample position of: (a) Bilayer and (b) Multilayer.

The deposition rates, calculated by the respective film thickness and corresponding deposition time, were found to be 7 and 6.7 nm/min for the TiAlN and CrAlN layer, respectively.

6.2 Film Adhesion

The adhesion of the Bi- and Multilayer was classified, according to VDI guideline 3842 [49], using Fig. 5.3 and the results are summarized in Table 6.1.

Table 6.1: Film adhesion classes HF as determined by the Rockwell C indentation test for the Bilayer and the Multilayer on the cemented carbide disks.

Position	**1**	**2**	**3**	**4**	**5**
HF Bilayer	2-3	2-3	2-3	2	2
HF Multilayer	2	2	2	2	2

Film adhesion is generally good, but not excellent, for both, Bilayer and Multilayer, as adhesion classes between HF2 and HF3 could be obtained.

6.3 Chemical Composition

The results of the investigation of the chemical composition by EDX measurements for the Bi- and Multilayer are summarized in Fig. 6.1. The N-content for each Bilayer sample is constant at approximately 50 at.% and corresponds, thus, to a stoichiometric composition. The Al/(Al+Cr) atomic-ratio increases from 0.21 for position 1 up to 0.46 for position 15. Four samples of the Multilayer were investigated, but determining the chemical composition by EDX is difficult, as the characteristic lines of Ti and N overlap. Furthermore, the Al-signal can not unambiguously be assigned to the CrAlN or TiAlN layers. Thus, approximate values for the Al/(Al+Cr) atomic-ratio of the CrAlN layers of the Multilayer were calculated. There, first the deposition rate of TiAlN and CrAlN was calculated, using the respective film thickness and deposition time of the Bilayer. According to the thus known fractions of both layers, the Al-content and thus the Al/(Al+Cr) atomic-ratio was calculated. The obtained values are in good agreement with those found on the Bilayer (see Fig. 6.2), with slight deviations at higher Al-contents.

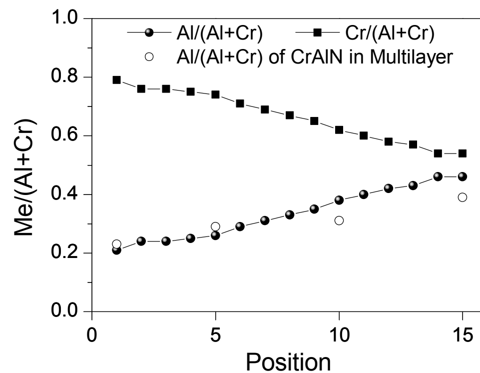

Fig. 6.2: Me/(Al+Cr) atomic-ratio of the Bilayer and Al/(Al+Cr) atomic-ratio of the CrAlN layers in the Multilayer, depending on the position of the SNUN samples.

6.4 Microstructure and Morphology

The XRD patterns of the Bilayer and the Multilayer samples are shown in Fig. 6.3. Due to the gracing incidence of 2°, the XRD patterns of the Bilayer mainly show peaks of the CrAlN top-layer. The peak positions for the cubic CrN, the cubic AlN and the cubic TiN phases stated in the JCPDS data base are plotted as dashed lines. Furthermore, an uncoated SNUN

sample was measured and the detected WC peaks are plotted as dashed lines. The detected (111), (200) and (220) peaks of the cubic CrN phase for both, Bilayer and Multilayer are shifted to higher 2θ-values when the Al-content is increased.

(a)

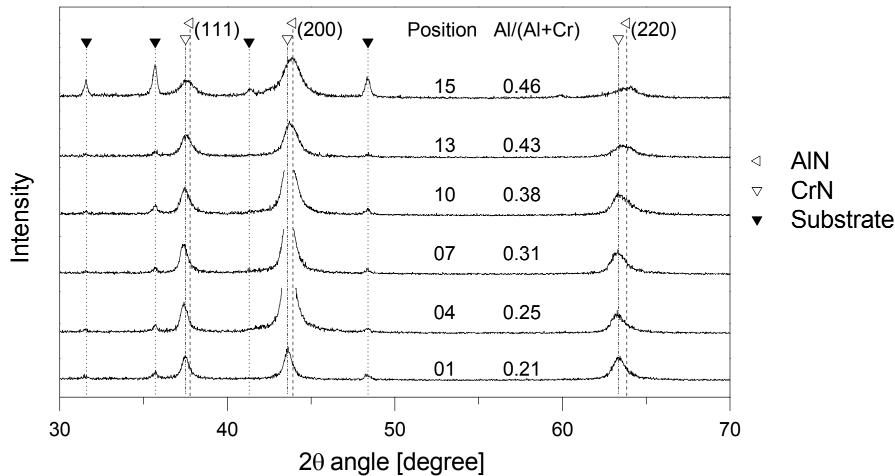

(b)

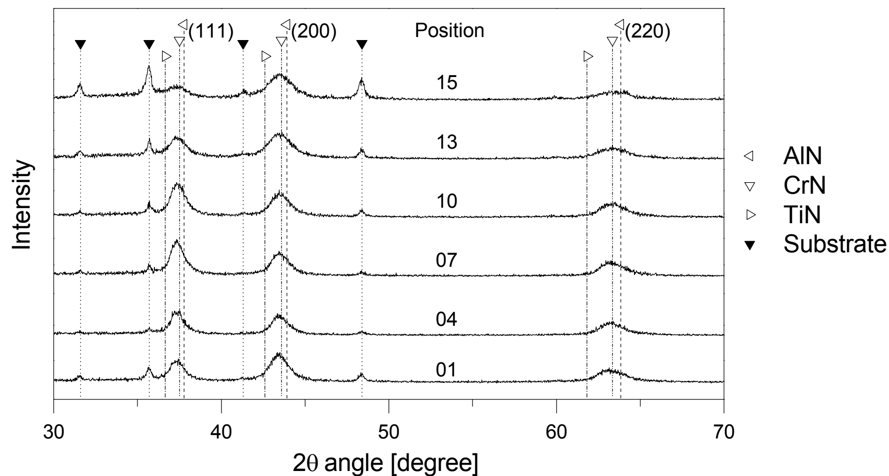

Fig. 6.3: Gracing incidence XRD patterns investigated on the SNUN samples of: (a) Bilayer and (b) Multilayer.

The (200) peaks show their highest intensities in case of the Bilayer and are most pronounced for Al/(Al+Cr) ratios between 0.25 and 0.38. For the Multilayer, the (111) and (200) peaks show more or less comparable intensities.

The film morphology was investigated by means of SEM on freshly broken Bi- and Multilayer SNUN samples. In Fig. 6.4, the SEM image of samples 1 and 15 of the Bi- and Multilayer are shown. The Al/(Al+Cr) atomic-ratio for positions 1 and 15 is 0.21 and 0.46

for the Bilayer and 0.23 and 0.39 for the Multilayer, respectively. For all films a dense, fibrous structure is observable that corresponds to the Zone T growth of the SZM of Thornton [26]. Furthermore, it is recognizable that the TiAlN base layer is approximately twice as thick as the respective top-layer.

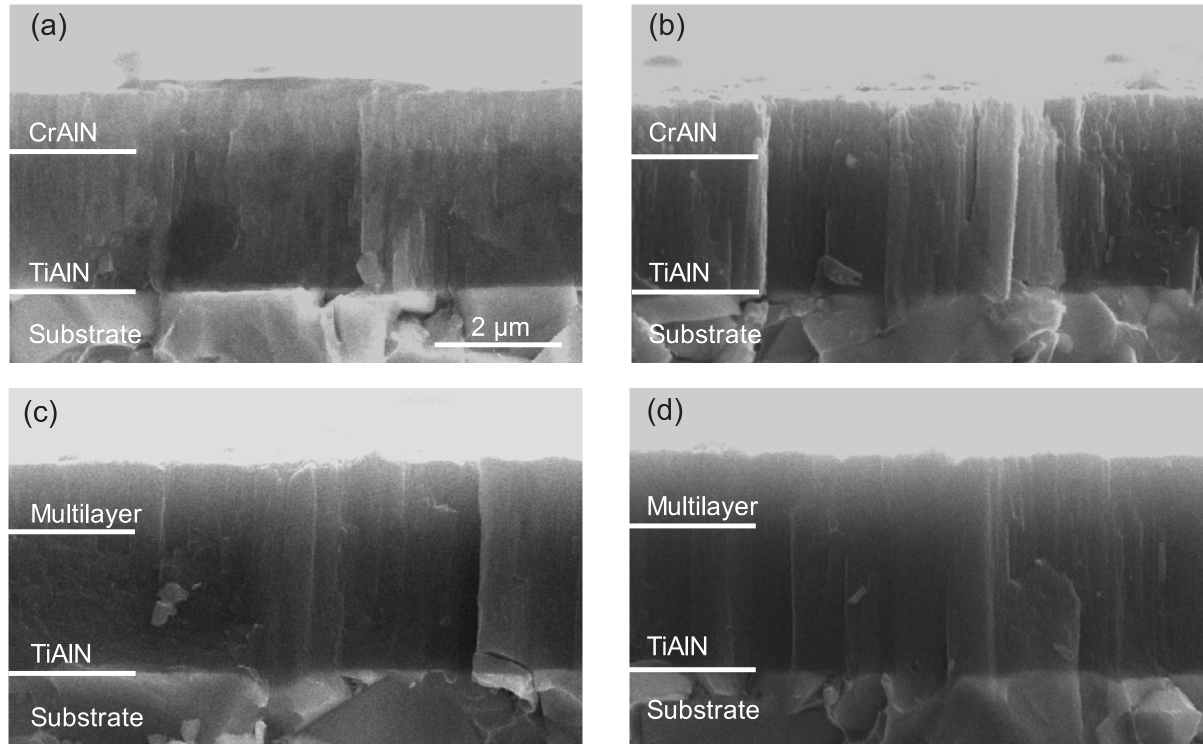

Fig. 6.4: SEM fracture cross-section of the: Bilayer 1 (a), Bilayer 15 (b), Multilayer 1 (c) and Multilayer 15 (d) deposited on SNUN samples. The corresponding Al/(Al+Cr) ratios are: 0.21 (a), 0.46 (b), 0.23 (c) and 0.39 (d).

6.5 Residual Stress

The change in residual stresses for the Bilayer and Multilayer, measured on Si-samples, is shown in Fig. 6.5. For the Bilayer, the obtained values range between -0.4 GPa for the highest compressive stresses and 0.1 GPa for the highest tensile stresses. The obtained values for the Multilayer are all in the compressive stress range and change from -0.84 GPa to -0.2 GPa. For both coating types, stress values are slightly higher for the samples positioned in front of the upper and lower areas of the Al/Cr segmented targets.

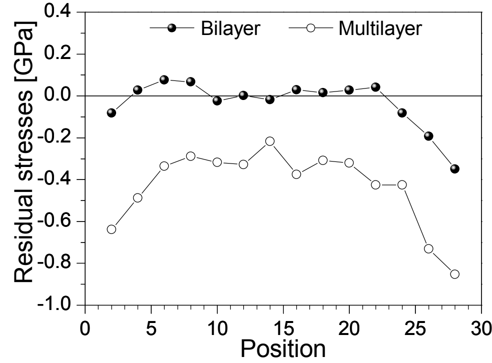

Fig. 6.5: Residual stresses of the Bilayer and Multilayer as a function of the Si-sample position.

6.6 Hardness and Young's Modulus

The hardness and Young's moduli, measured on SNUN samples, are shown in Fig. 6.6. For the Bilayer, H values of 18 - 30 GPa were measured, whereas the highest H was found on sample 14 with an Al/(Al+Cr) ratio of 0.31. In case of the Multilayer, H varies between 27 and 33 GPa. Here, the highest H was measured on sample 18 with an Al/(Al+Cr) ratio of approximately 0.31. Young's moduli for the Bilayer are in the range of 280 - 370 GPa, and for the Multilayer between 320 and 370 GPa.

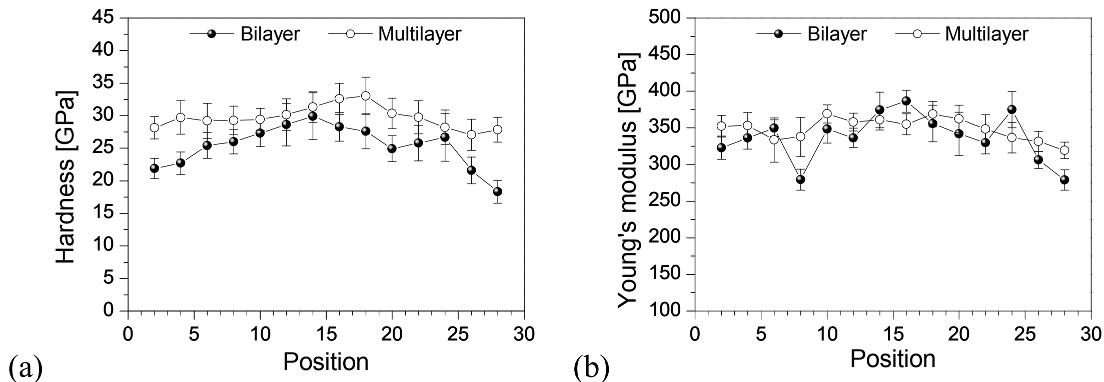

Fig. 6.6: Hardness (a) and Young's modulus (b) for the Bilayer and the Multilayer depending on the SNUN-sample position.

6.7 Tribological Properties

Tribological investigations using a ball on disk test against Al_2O_3 were done for the Bilayer and Multilayer samples at room temperature, 500 and 700°C. The development of the friction coefficient as a function of the sliding distance as well as the shape of the wear track, obtained for five different compositions is shown in Figs. 6.7 and 6.8. The Al/(Al+Cr) atomic-ratio of the Bilayer films on the cemented carbide disks were assumed to be equal to

that of the SNUN samples, that were deposited nearly at the same height than the center of the disks. Due to the size of the cemented carbide disks, however, a compositional gradient on the samples may be expected. As for the Multilayer already the composition had to be estimated (see section 6.3), no further assumptions seemed to be feasible to give a composition.

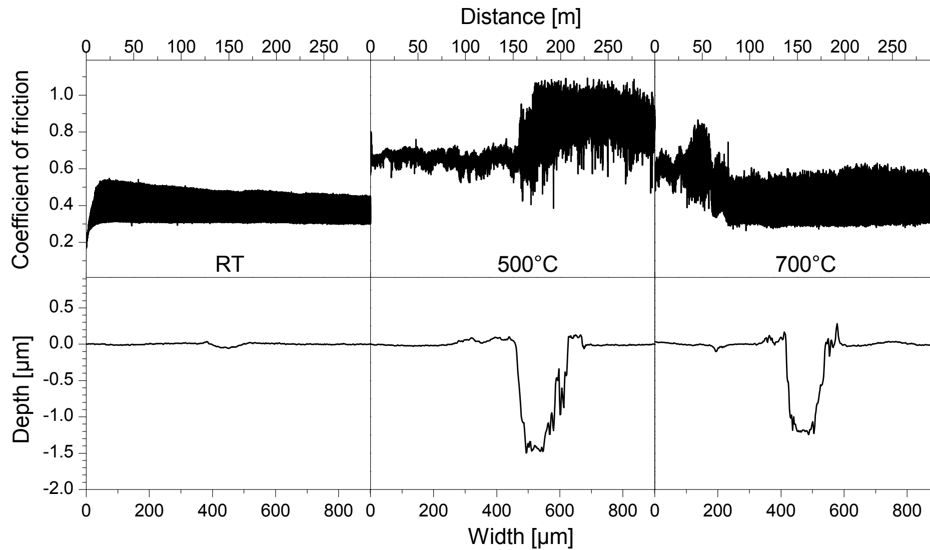

(a) Al/(Al+Cr)=0.26

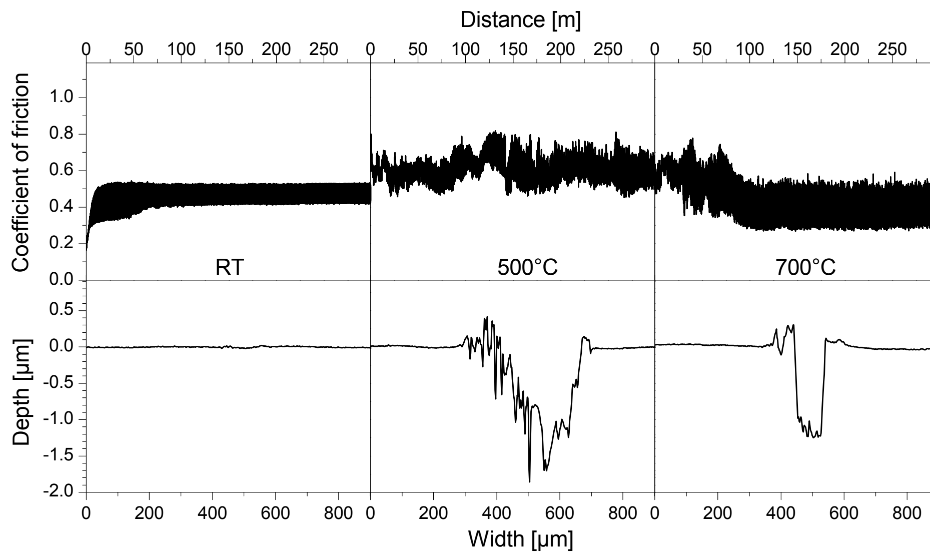

(b) Al/(Al+Cr)=0.31

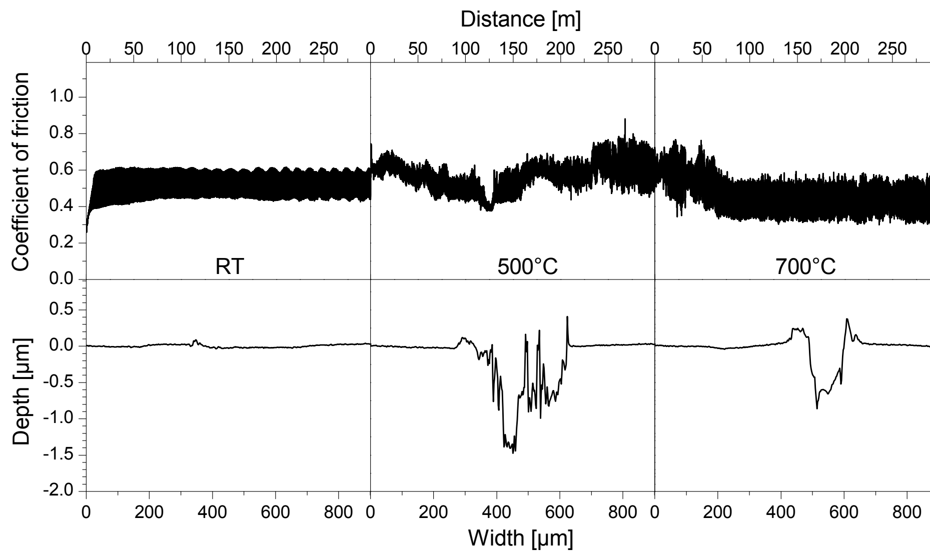

(c) Al/(Al+Cr)=0.36

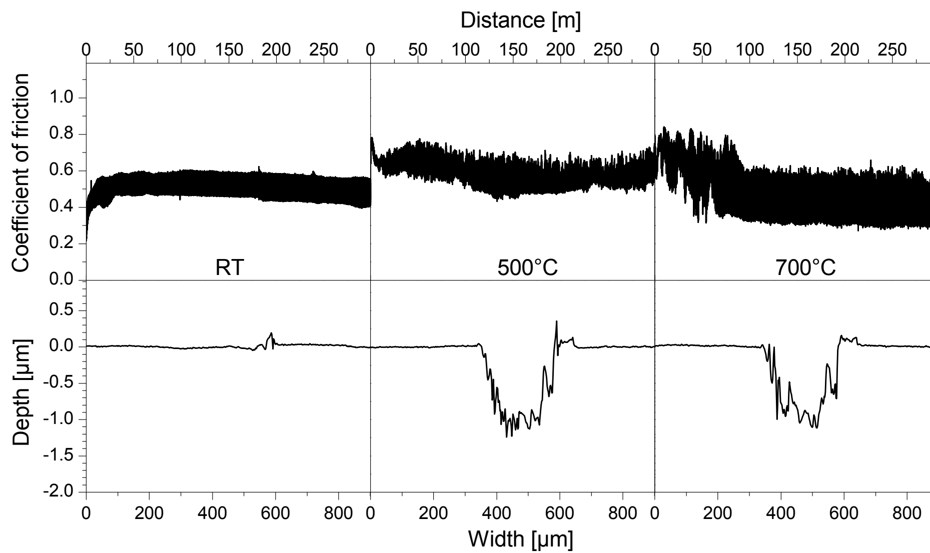

(d) Al/(Al+Cr)=0.40

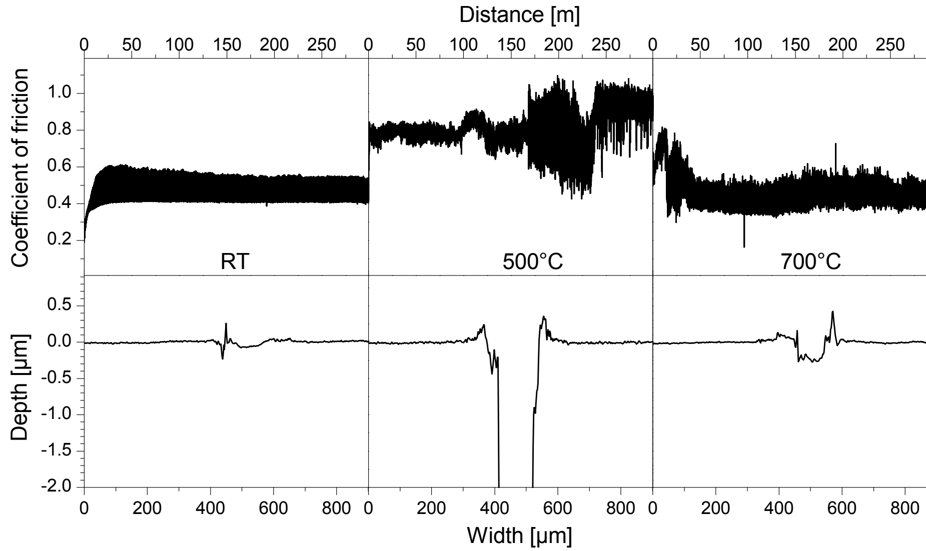

(e) Al/(Al+Cr)=0.43

Fig. 6.7: Friction coefficient as a function of the sliding distance and wear track profiles obtained at different temperatures for the Bilayer on cemented carbide disks for positions 1-5. The Al/(Al+Cr) atomic-ratios are also given.

For all investigations carried out at room temperature, μ stays more or less constant in a steady-state regime after a running in period of 25 - 30 m. The values of μ of the Bilayer are between 0.4 - 0.5, whereas the lowest one was found for the Bilayer position 1 with an Al/(Al+Cr) ratio of 0.26 (compare Fig. 6.7). At 500°C, a higher μ of about 0.7 is observed for the Bilayer samples, in the early stage of the test. Moreover, the curve shows a jagged characteristics, where for samples 1 and 5 μ increases slightly after a sliding distance of 150 m and broader scattering could be observed. At 700°C, μ stays more or less constant at approximately 0.4 - 0.45, after reaching a sliding distance of 50 - 60 m.

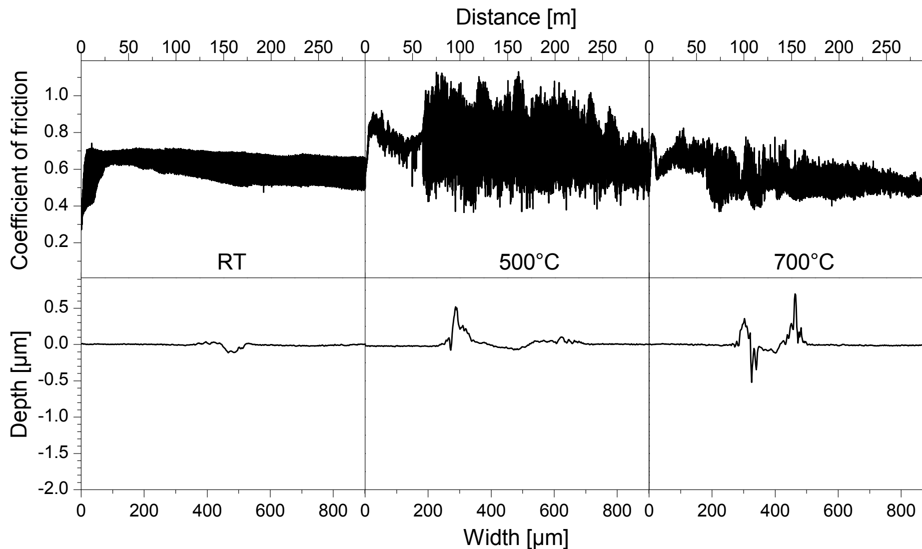

(a) Position 1

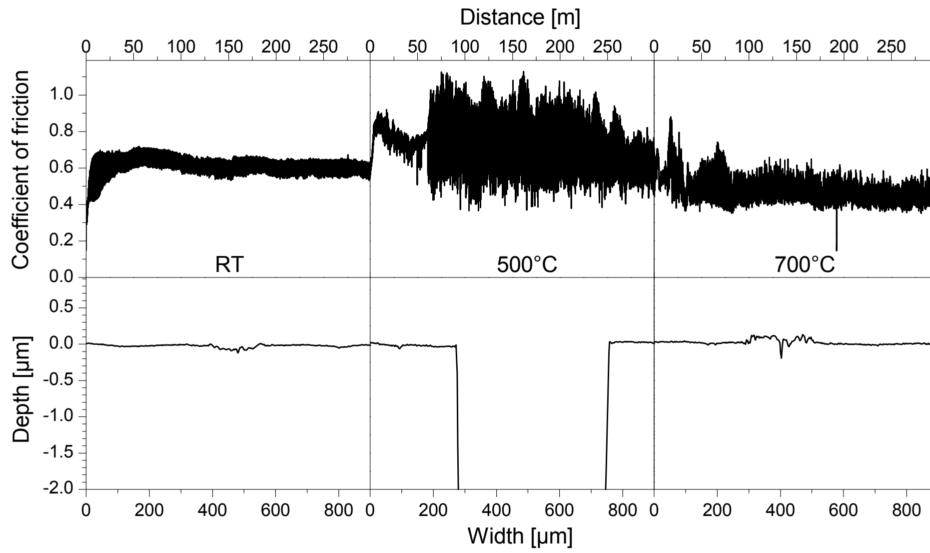

(b) Position 2

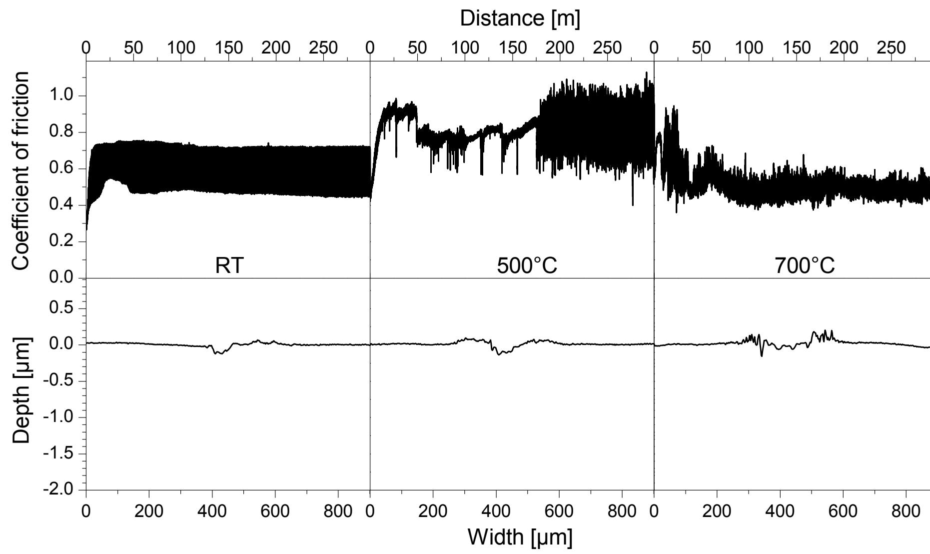

(c) Position 3

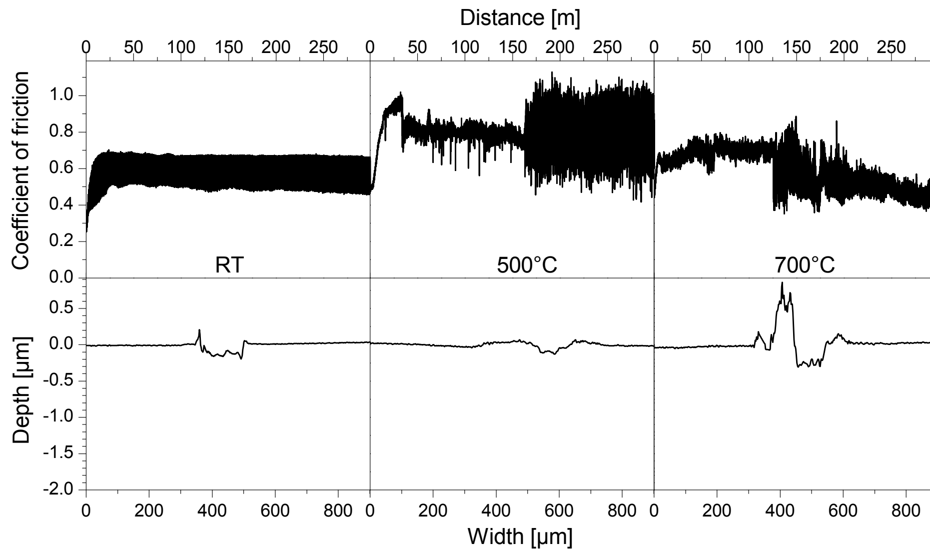

(d) Position 4

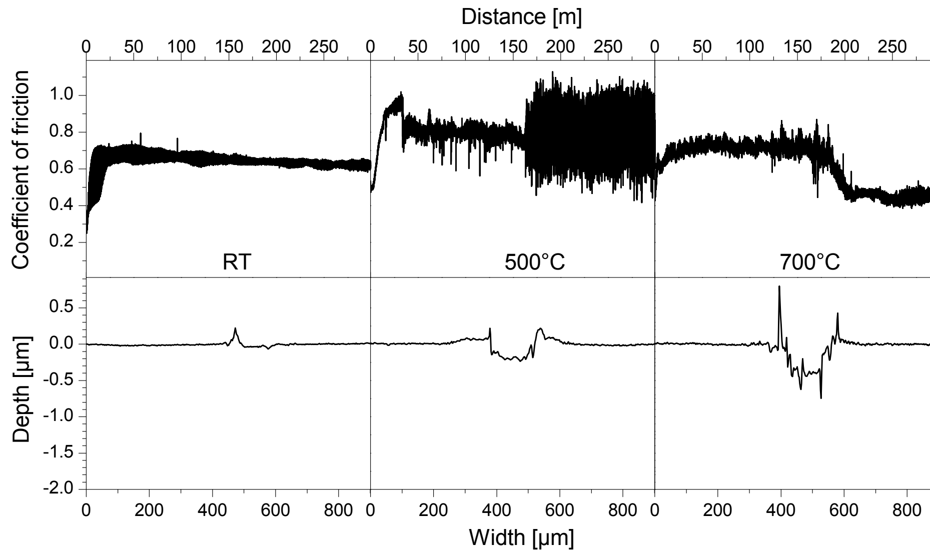

(e) Position 5

Fig. 6.8: Friction coefficient as a function of the sliding distance and wear track for different temperatures obtained for the Multilayer on cemented carbide disks of positions 1-5.

For the multilayer, μ values of around 0.6 were found at room temperature, i.e slightly higher than for the Bilayer (compare Figs. 6.7 and 6.8). Multilayer 5 shows the lowest scattering of μ. At 500°C, μ increases rapidly within the running-in period reaching values of 0.9 - 1.0. After that, μ decreases to 0.7 - 0.8 until above 80 m for positions 1 and 2 and 150 m for positions 3, 4 and 5 broad scattering of the friction coefficient is observed. At 700°C, positions 1, 2 and 3 show a similar behavior as the Bilayer at 700°C, with μ values around 0.5 after 50 - 60 m. For samples 4 - 5, μ increases during the running-in period reaching values of 0.7 and than decreases after 150 m to 0.4 - 0.5.

A low wear track depth of less than 0.1 µm was observed on every Bi- and Multilayer sample tested at room temperature. At elevated temperatures, the films were on the one hand partially totally worn by film delamination (see Fig. 6.9).

Substrate material visible, due to the totally worn film.

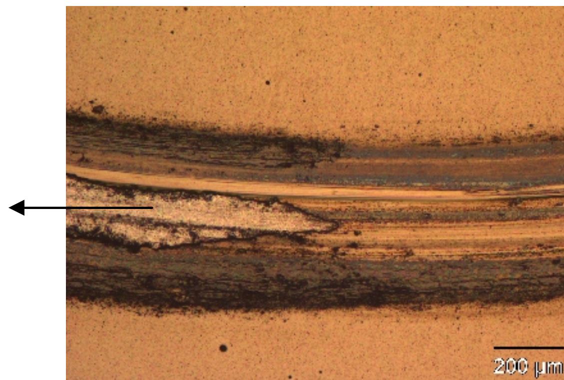

Fig. 6.9: Optical micrograph of the wear track on the Bilayer position 1 with an Al/(Al+Cr) atomic-ratio of 0.26, tested at 500°C, which shows the transition from slight wear to a totally worn film.

On the other hand, on not delaminated areas the wear track depth reaches values of not even 1.5 µm for the Bilayer and 0.5 µm for the Multilayer, respectively (compare Figs. 6.7 and 6.8). The Bilayer sample 5 and Multilayer sample 2 could not withstand the tribological load at 500°C and the film was totally worn through.

The wear coefficient, *K,* was calculated for all samples in the areas were the film is not delaminated and is 1.8 - $3.2 \cdot 10^{-16}$ m^3/Nm for the Bilayer and 2.6 - $5.3 \cdot 10^{-16}$ m^3/Nm for the Multilayer at room temperature (Fig. 6.5). At 500°C, *K* is 3.9 - $5.7 \cdot 10^{-15}$ m^3/Nm for the Bilayer and 2.1 - $5.9 \cdot 10^{-16}$ m^3/Nm for the Multilayer. At 700°C, *K* values in the range of 0.74 - $3.18 \cdot 10^{-15}$ m^3/Nm for the Bilayer and 1.4 - $7.6 \cdot 10^{-16}$ m^3/Nm for the Multilayer were calculated.

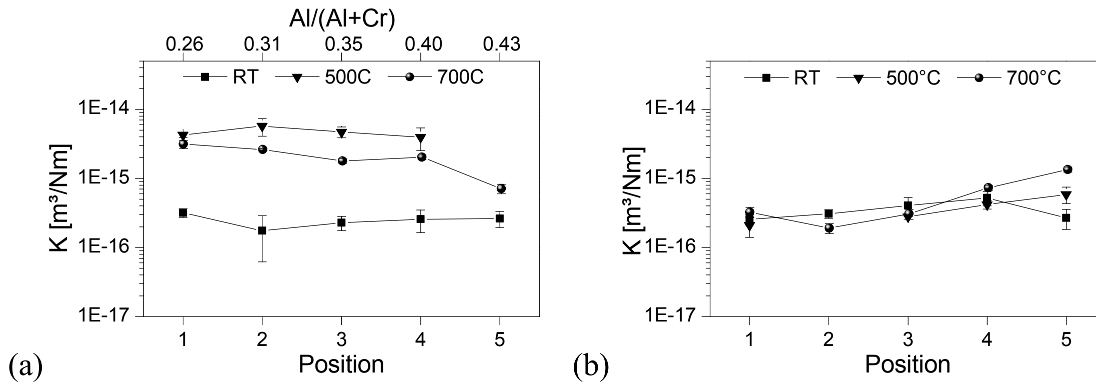

Fig. 6.10: Wear coefficients investigated at different temperatures for the Bilayer (a) and the Multilayer (b).

7 Discussion

7.1 Deposition – structure – property relations

An understanding of the relation between deposition process parameters, thin film growth and resulting microstructure, as well as mechanical and tribological properties, allows the effective control of the sputter deposition process and subsequently the adjustment of desired properties. Thus, in the following section an attempt is being made to interpret and discuss the obtained results.

The mean film thickness of both, Bilayer and Multilayer is almost the same, with values of 3.4 ± 0.2 µm and 3.3 ± 0.2 µm, respectively, whereas the thickness of the TiAlN base layer is constant with approximately 2 µm. Furthermore, the deposition rates determined for the central areas of the targets, were found to be nearly the same for TiAlN and CrAlN with values of 7 nm/min and 6.7 nm/min, respectively. However, for the top-layers slightly lower film thicknesses were determined on the samples positioned in front of the upper and lower areas of the segmented Cr/Al targets (see Fig. 6.1). This can be related to the geometrical arrangement of the substrates with respect to the segmented Cr and Al targets, as the samples were positioned over nearly the total target length, shown in Fig. 7.1. Film adhesion, however, is nearly constant for all samples and in the range between HF 2 and HF 3.

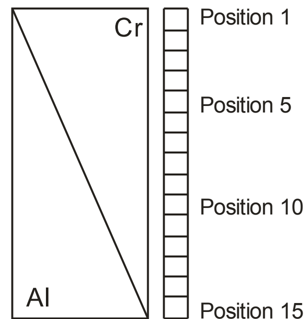

Fig. 7.1: Arrangement of the SNUN samples with respect to the segmented Cr and Al targets.

The Bilayer coatings consist solely of the single phase cubic $Cr_{1-x}Al_xN$ solid solution; there are no peaks of the hexagonal phase recognizable (compare Fig. 6.3). The observed shift of the peaks from positions close to CrN to higher 2θ-values, from the lowest to the highest Al-content, is attributed to the decrease in lattice parameter of $Cr_{1-x}Al_x$ N, since Cr atoms are substituted by smaller Al atoms [54]. Since the composition of the CrAlN layers varies, the detected peaks are located in between the peaks of cubic CrN and cubic AlN, with increasing shift to the AlN position for higher Al-content. For the Bilayer, the (200) peak is much

higher than the (111) peak, indicating a 100 orientation. This is in good accordance with Barshilia *et al.* [55], who also found a 100 orientation for CrAlN layers with an Al/(Al+Cr) atomic-ratio of 0.5. Furthermore, the texture of such transition metal nitride coatings can also be influenced by the ion to metal flux (J_i/J_{me}) in the plasma. A low J_i/J_{me} ratio will result in preferred 111 orientations, whereas a decrease of J_{me} (i.e. a low growth rate) can result in a preferred 100 texture [24, 56].

As expected also for the Multilayer the peaks of the cubic CrN phase are shifted to higher 2θ-values. The detected (111) peaks are nearly as intense as the (200) peaks, thus no preferred orientation is observable (see Fig. 6.3). This might be explained by the substrate rotation, where the samples rotate from the plasma in front of the TiAl targets to that in front of the segmented Cr/Al targets. Thus, the nucleation step starts all over again and island growth and subsequently the development of a continuous structure is interrupted periodically [24]. Furthermore, differences in plasma-intensity in front of the different targets, due to the larger surface of the TiAl targets and the therefore higher cathode currents, might lead to variations in ion bombardment, subsequently leading to random orientation.

Due to the arrangement of the samples with respect to the Cr/Al segmented targets (see Fig. 7.1), also CrAlN films with an Al-content above 0.5 were expected, but the highest reached Al-content is 0.46. This might be an effect of the formation of an AlN layer on the target [1, 10]. While on the Cr target a CrN layer can also be formed, the stability of the AlN layer is assumed to be much higher. This is corroborated by the respective formation enthalpies. They are -117 kJ/mol for CrN and -318 kJ/mol for AlN [57]. The more negative the enthalpy of formation, the more stable is the compound and the more energy is necessary to destroy it [58]. Thus, more Cr will be sputtered than Al. This is even more pronounced by the different sputtering yields (atoms/incident ion) of Cr and Al. For the same kinetic energy of the incident Ar^+ ions, the sputtering yield is slightly higher for Cr than for Al (see Fig. 7.2) [59]. For the TiAlN base layer and the layers within the Multilayer, an Al/Ti ratio of 63:37 is expected. This is supported by Schalk [60], who deposited TiAlN layers from the same targets, with similar deposition parameters.

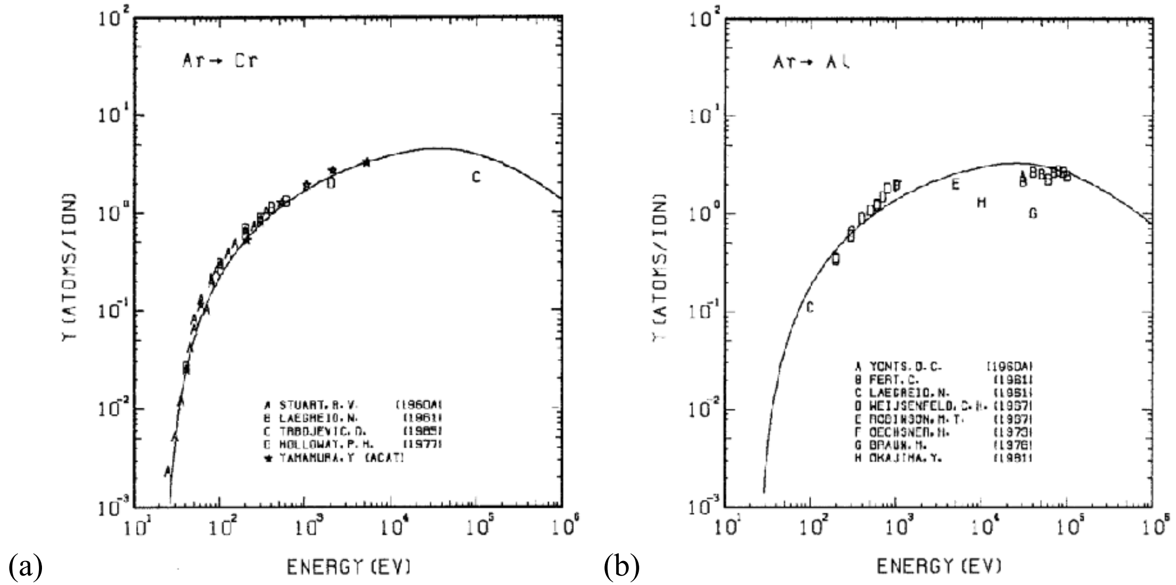

Fig. 7.2: Sputtering yield of (a) Cr with Ar^+ and (b) Al with Ar^+ [59].

Relatively low residual stresses were found for the Bilayer, between compressive -0.4 GPa and slightly tensile 0.1 GPa values, and the Multilayer, between -0.84 GPa and -0.2 GPa. The highest compressive stresses were observed on the upper and lower positions (compare Fig. 6.8). Compressive stresses are generated by energetic bombardment of the growing film, due to the applied bias voltage, leading to lattice distortion [61]. The higher compressive stresses on the Cr-rich samples might be explained by the low Al-content. In the cubic CrAlN phase, Cr atoms are substituted by the smaller Al atoms, thus generating tensile stresses [41]. Furthermore, stresses are highly depending on film thickness, as the structure alters in different stages of Zone T film growth and subsequently thickness-depending growth stress components are generated [61]. Moreover, the higher compressive stresses on the upper and lower positions might be a result of the lower film thickness and the subsequently lower metal flux J_{me} for these positions, leading to an increased J_i/J_{me} ratio. This increasing J_i/J_{me} ratio is known to lead to decreasing tensile stresses and increasing compressive stresses [62].

The hardness and the Young's modulus for the Bilayer increase due to the increasing Al-content, until reaching a maximum value at an Al/(Al+Cr) atomic-ratio of about 0.3 (compare Fig. 6.6). This equates to an Al/Cr ratio of approximately 0.4 - 0.5, that has also been found by Ding *et al*. [3] for the composition were highest hardness could be observed. The increasing hardness can be explained by the dissolution of Al atoms in the cubic CrN lattice. Consequently, strain is induced in the film, hindering dislocation movement and subsequently increases the hardness [63]. The decrease observed for Al/(Al+Cr) atomic-

ratios above 0.3 can not be clarified up to now. A possible reason could be an increasing defect density due to Al incorporation, leading to highly distorted crystal structures. The hardness of the Multilayer shows a similar behavior, but with very low differences in hardness values (see Fig. 6.6). The obtained values of 27 - 33 GPa seem to be mainly influenced by the TiAlN layers and are in good accordance with the values found by Schalk for TiAlN monolayer coatings [60].

The Bilayers yield excellent performance during tribological investigations performed at room temperature, with values between 0.4 and 0.5 for the coefficient of frictions (see Fig. 6.7). It appears that the increasing Al-content does not influence the coefficient of fricition significantly. The coefficient of friction of the Multilayer, as already the hardness, is strongly affected by the TiAlN layers. Since the coefficient of friction of TiAlN at room temperature has been reported to be higher than for CrAlN [60], slightly higher values of about 0.6 have been obtained for the Multilayer than for the Bilayer (compare Fig. 6.8). The wear coefficients at room temperature are comparable for the Bi- and the Multilayer, with values of $1.8 - 3.2\cdot10^{-16}$ and $2.6 - 5.3\cdot10^{-16}$ m^3/Nm, respectively (see Fig. 6.10). The dominating wear mechanism at room temperature is abrasive wear whereas with increasing Al-content also adhesive wear is observed (see Fig. 6.7). Here, the transfer material might be material of the Al_2O_3-ball or film material that was transferred onto the ball and then retransferred [38, 39]. The tribological performance at higher temperatures might be influenced negatively by the not perfect film adhesion. In particular, the Bilayer position 5 with an Al/(Al+Cr) ratio of approximately 0.43 and the Multilayer position 2 failed completely during the tests. The partial failure of all the other films could also be explained by adhesion problems. The jagged characteristics of the friction curve at 500°C (compare Fig. 6.7) is an indication for abrasive particles that piled up in front of the Al_2O_3-ball, subsequently leading to higher friction values. When breaking free, the coefficient of friction decreases rapidly again [38, 39]. The lower coefficient of friction measured at 700°C than at 500°C is a result of the beginning formation of protecting oxide layers. It has been reported, that the oxide scale formed on CrAlN layers is a mixed Cr_2O_3-Al_2O_3 layer [64]. Thus, it can be assumed that this is also valid for the oxide scale formed on the Bilayer. The layer formation is determined by Cr and Al outward diffusion, whereas the Cr outward diffusion rate is higher than that for Al. Thus, the surface near part is Cr-rich and the underneath part is Al-rich [64]. The oxide scale on TiAlN is a bilayer, where the upper sub-layer is mainly Al_2O_3 and the lower one TiO_2 [65]. Comparing the hardness of the oxide scales shows, that Al_2O_3 is harder than Cr_2O_3, which leads to a possible explanation for the better wear behaviour of the Multilayer than the

Bilayer at high temperatures. At 700°C the wear rate of the Multilayer with values of 1.4 - $7.6\cdot10^{-16}$ m^3/Nm is similar to that at room temperature, whereas the wear coefficient for the Bilayer is about 0.74 - $3.18\cdot10^{-15}$ m^3/Nm and thus, higher than at room temperature. At high-temperatures abrasive and adhesive wear is observable on each sample (see Figs. 6.8 and 6.9) [38, 39]. Also here, the transfer material might be material of the Al_2O_3-ball or of the film itself.

7.2 Comparison between sputtered and arc evaporated CrAlN films

Despite the low deposition rate, sputtered CrAlN layers exhibit advantages over e.g. arc-evaporated CrAlN films. In Table 7.1 several properties of the films investigated within this thesis are compared to properties of arc-evaporated CrAlN films with an Al/(Al+Cr) atomic-ratio of approximately 0.4. Typically used $Cr_{1-x}Al_xN$ films have higher Al/(Al+Cr) atomic-ratios than 0.4 - 0.5, but as the highest ratio obtained in the present work is 0.46, papers published by Reiter [64] and Franz [66] were used as references. They cover a wide composition range including Al/(Al+Cr) ratios of 0.4 – 0.5.

Table 7.1: Comparison of properties of arc-evaporated and sputtered CrAlN films.

	Arc-evaporation		Literature	Sputter deposition
Al/(Al+Cr) atomic-ratio	0.4	0.46	[65]/[63]	0.43
Deposition rate [nm/min]	50		[65]	7
Preferred orientation	None		[65]	100
Friction coefficient at RT against Al_2O_3 [-]	0.7		[65]	0.5
Friction coefficient at 700°C [-]	0.6		[65]	0.5
Wear coefficient at RT [m^3/Nm]	$2\cdot10^{-16}$		[65]	$2\cdot10^{-16}$
Wear coefficient at 700°C [m^3/Nm]	$3\cdot10^{-14}$		[65]	$6\cdot10^{-16}$
Hardness [GPa]		38	[63]	30

8 Summary and Conclusions

Within the scope of this thesis, segmented triangle-like Cr and Al targets were used for industrial-scale sputter deposition of $Cr_{1-x}Al_xN$ films, with various compositions to study the resulting structure-property relation. Two different film architectures have been synthesized on cemented carbide and Si (100) substrates by reactive unbalanced magnetron sputtering. Both, the TiAlN-CrAlN Bilayer and Multilayer were deposited on TiAlN base layers, grown from homogenous TiAl targets with an Al-content of 60 at.%.

The achieved film thicknesses for the Bilayer and the Multilayer, after 510 min and 405 min deposition time, are 3.4 ± 0.2 µm and 3.3 ± 0.2 µm, respectively, with comparable moderate adhesion to the cemented carbide disks. Energy-dispersive x-ray spectroscopy measurements on both film systems, showed Al/(Al+Cr) atomic-ratios of the $Cr_{1-x}Al_xN$ layers between 0.21 and 0.46 and consequently, a single-phase cubic film structure was observed. The Bilayer showed a 100 and the Multilayer no preferred orientation.
For the Bilayer residual stresses are quite low in the range between -0.4 and 0.1 GPa, compared to other film systems. Stresses of the Multilayer are slightly higher than for the Bilayer, with values between -0.84 and -0.2 GPa. In both cases highest compressive stresses were observed for the samples positioned in front of the upper and lower areas of the Al/Cr segmented targets. For the Bi- and the Multilayer, hardness values of 18 - 30 GPa and 27 - 33 GPa, respectively, were observed. Here, for both film systems, highest values were found on the samples positioned in front of the central area of the Cr/Al targets. The Young's moduli showed a similar trend, with higher values for the Multilayer than for the Bilayer. At room temperature, the Bilayer showed excellent performance during tribological investigations with friction coefficients in the range of 0.4 - 0.5 and wear coefficients of $1.8 - 3.2 \cdot 10^{-16}$ m^3/Nm. At 500°C, both film architectures showed worst performance. At 700°C, however, the Multilayer showed better friction and wear behavior than the Bilayer, with friction coefficients of 0.5 - 0.6 and wear coefficients in the range of $0.74 - 3.18 \cdot 10^{-16}$ m^3/Nm.

In conclusion, it has been shown that the Bilayer exhibit increased tribological properties during room temperature testing, compared with the Multilayer. However, by increasing the temperature during tribological investigations, the multilayered films indicate less coating wear. Furthermore, it can be said that the segmented targets are a good opportunity to analyze the structure-property evolution in an industrial-scaled sputtering system, over a

broad compositional range, in one single deposition run. Nevertheless, there seems to be further potential to achieve even higher compositional variations by e.g. using such targets with a length of 500 mm.

References

[1] M. Brizuela, A. Garcia-Luis, I. Braceras, J.I. Onate, J.C. Sanchez-Lopez, D. Martinez-Martinez, C. Lopez-Cartes, A. Fernandez, Magnetron sputtering of Cr(Al)N coatings: Mechanical and tribological study, Surf. Coat. Technol. 200, 192-197, 2005.

[2] R.F. Bunshah, Handbook of deposition technologies for films and coatings, Noyes Publications, New Jersey, 1994.

[3] X.Z. Ding, X.T. Zeng, Structural, mechanical and tribological properties of CrAlN coatings deposited by reactive magnetron sputtering, Surf. Coat. Technol.200, 1372-1376, 2005.

[4] M. Okumiya, M. Griepentrog, Mechanical properties and tribological behavior of TiN-CrAlN and CrN-CrAlN multilayer coatings, Surf. Coat. Technol. 112, 123-128, 1999.

[5] K. Bobzin, E. Lugscheider, R. Nickel, P. Immrich, (Cr1-x,Alx)N Ein Review über ein vielseitig einsetzbares Schichtsystem, Mat.-wiss. U. Werkstofftech. 37, 833-841, 2006.

[6] Fr.-W. Bach, A. Laarmann, T. Wenz, Modern Surface Technology, Wiley-VCH, Weinheim, 2006.

[7] Fr.-W. Bach, T. Duda, Moderne Beschichtungsverfahren, Wiley-VCH, Weinheim, 2000.

[8] G. Kienel, K. Röll, Vakuumbeschichtung 2, Verfahren und Anlagen, VDI Verlag, Düsseldorf, 1995.

[9] W.D. Westwood, Sputter Deposition, Wiley, New York, 2003.

[10] D.M. Mattox, Handbook of Physical Vapor Deposition (PVD) Processing, Noyes Publications, New Jersey, 1998.

[11] H. Frey, Vakuumbeschichtung 1, Plasmaphysik – Plasmadiagnostik – Analytik, VDI Verlag, Düsseldorf, 1995.

[12] R.A. Haerfer, Oberflächen- und Dünnschicht- Technologie, Teil I, Beschichtung von Oberflächen, Springer Verlag, Berlin, Heidelberg, 1987.

[13] W.D. Sproul, High-rate reactive DC magnetron sputtering of oxide and nitride superlattice coatings, Vacuum 51 (4), 641-646, 1998.

[14] M. Ohring, The Material Schience of Thin Films – deposition and structure, Academic Press, San Diego, Second edition, 2002.

[15] W.D. Sproul, D.J. Christie, D.C. Carter, Control of reactive sputtering processes, Thin Solid Films 491, 1-17, 2005.

[16] R.D. Arnell, P.J. Kelly, Recent advances in magnetron sputtering, Surf. Coat. Technol. 112, 170-176, 1999.

[17] P.J. Kelly, R.D. Arnell, Magnetron sputtering: a review of recent developments and applications, Vacuum 56, 159-172, 2000.

[18] E. Lugscheider, O. Knotek, F. Löffler, C. Barimani, S. Guerreiro, H. Zimmermann, Deposition of arc TiAlN coatings with pulsed bias, Surf. Coat. Technol. 76-77, 700-705, 1995.

[19] M. Griepentrog, B. Mackrodt, G. Mark, T. Linz, Properties of TiN hard coatings prepared by unbalanced magnetron sputtering and cathodic arc deposition using a uni- and bipolar pulsed bias voltage, Surf. Coat. Technol. 74-75, 326-332, 1995.

[20] H. Lüth, Solid Surfaces, Interfaces and Thin Films, Springer Verlag, Berlin, Heidelberg, 2010.

[21] K. Wasa, M. Kitabatake, H. Adachi, Thin Film Materials Technology, Sputtering of Compound Materials, Springer Verlag, Berlin, Heidelberg, 2004.

[22] M. Moser, Structural Evolution of Protective coatings for gamma-TiAl based alloys, PhD Thesis, Montanuniversität Leoben, 2008.

[23] R. Messier, A.P. Giri, R.A. Roy, Revised structure zone model for thin film physical structure, J. Vac. Sci. Technol. A, 2(2), 500-503, 1984.

[24] I. Petrov, P.B. Barna, L. Hultman, J.E. Greene, Microstructural evolution during film growth, J. Vac. Sci. Technol. A, 21(5), 117-128, 2003.

[25] B.A. Movchan, A.V. Demchishin, Study of the structure and properties of thick vacuum condensates of nickel, titanium, tungsten, aluminum oxide and zirconium dioxide, Phys. Met. Metallogr. 28, 653-660, 1969.

[26] J.A. Thornton, The microstructure of sputter-deposited coatings, J. Vac. Sci. Technol. A, 4(6), 3059-3065, 1986.

[27] P.B. Barna, M. Adamik, Fundamental structure forming phenomena of polycrystalline films and the structure zone models, Thin Solid Films 317, 27-33, 1998.

[28] B. Rother, J. Vetter, Plasmabeschichtungsverfahren und Hartstoffschichten, Deutscher Verlag für Grundstoffindustrie, Leipzig, 1992.

[29] K.-D. Bouzakis, G. Skordaris, N. Michailidis, I. Mirisidis, G. Erkens, R. Cremer, Effect of film ion bombardment during the pvd process on the mechanical properties and cutting performance of TiAlN coated tools, Surf. Coat. Technol. 202, 826-830, 2007.

[30] G. Kienel, Vakuumbeschichtung 3, Anlagenautomatisierung, Mess- und Analysetechnik, VDI Verlag, Düsseldorf, 1994.

[31] G.M. Pharr, W.C. Oliver, Measurement of thin film mechanical properties using nanoindentaion, Mrs Bulletin, 1992.

[32] http://www.ibisonline.com.au/IBIS_HandbookofNanoindentation.html

[33] A.C. Fischer-Cripps, Critical review of analysis and interpretation of nanoinentation test data, Surf. Coat. Technol. 200, 4153-4165, 2006.

[34] Y. Paleau, Generation and evoulution of residual stresses in physical vapor deposited thin films, Vacuum 61, 175-181, 2001.

[35] I.M. Hutchings, Tribology: Friction and wear of engineering materials, Edward Arnold, London, 1992.

[36] K. Holmberg, A. Matthews, Coatings tribology, properties, techniques and applications in surface engineering, Elsevier Science, Amsterdam, 1994.

[37] E. Rabinowicz, Friction and Wear of Materials, 2nd edition, John Wiley & Sons, New York, 1995

[38] N.P. Suh, H.-C. Sin, The genesis of friction, Wear 69, 91-114, 1981.

[39] W.D. Münz, Titanium aluminium nitride films: A new alternative to TiN coatings, J. Vac. Sci. Technol. A 4(6), 2717-2725, 1986.

[40] S. PalDey, S.C. Deevi, Single layer and multilayer wear resistant coatings of (Ti,Al)N: a review, Material Science and Engineering A342, 58-79, 2003.

[41] M. Zhou, Y. Makino, M. Nose, K. Nogi, Phase transition and properties of TiAlN thin films prepared by r.f.-plasma assisted magnetron sputtering, Thin Solid Films 339, 203-208, 1999.

[42] C. Rebholz, H. Ziegele, A. Leyland, A. Matthews, Structure, mechanical and tribological properties of nitrogen-containing coatings prepared by reactive magnetron sputtering, Surf. Coat. Technol. 115, 222-229, 1999.

[43] H.A. Jehn, B. Rother, Preparation and concentration distribution of multilcomponent hard coatings, Int. J. Refract. Metals Hard Mater. 14, 87-95, 1996.

[44] J. Kolscheen, H.-R. Stock, P. Mayr, Substoichiometric titanium nitride coatings as machinable surfaces in ultraprecision cutting, Surf. Coat. Technol. 120-121, 740-745, 1999.

[45] A. Sugishima, H. Kajioka, Y. Makino, Phase transition of pseudobinary Cr-Al-N films deposited by magnetron sputtering method, Surf. Coat. Technol. 97, 590-594, 1997.

[46] F. Rovere, Theoretical and experimental assessment of Cr-Al-Y-N as protective coating for γ-TiAl based alloys, PhD Thesis, RWTH Aachen, 2010.

[47] P.H. Mayrhofer, A. Hörling, L. Karlsson, J. Sjölén, T. Larsson, C. Mitterer, L. Hultman, Self-organized nanostructures in the Ti-Al-N system, Appl. Phys. Lett. 83(10), 2049-2051,2003.

[48] P.H. Mayrhofer, Materials science aspects of nanocrystalline PVD hard coatings, PhD Thesis, Montanuniversität Leoben, 2001.

[49] H.-R. Stock, A. Schulz, DIN-Fachbericht 39: Charakterisierung dünner Schichten, 1. Auflage, in H. Jehn, G. Reiners, N. Siegel, editors, Beuth Verlag, Berlin, 1993.

[50] G.M. Pharr, W.C. Oliver, An improved technique for determining hardness and elastic modulus using load displacement sensing indentation experiments, J. Mater. Res. 7(6), 1564-1583, 1992.

[51] D. Winkler, Konzept und Realisierung eines thermisch unterstützen Meßverfahrens zur Bestimmung von Eigenspannungen in dünnen Schichten, Diplomarbeit, Montanuniversität Leoben, 1997.

[52] W.D. Nix, Mechanical properties of thin films, Metallurgical Transactions 20A, 1989-2217.

[53] T. Weirather, Hochtemperaturbeschichtung von $Ti_{1-x}Al_xN$ auf verschiedenen Schnellarbeitsstählen, Diplomarbeit, Montanuniversität Leoben, 2008.

[54] A. Kimura, M. Kawate, H. Hasegawa, T. Suzuki, Anisotropic lattice expansion and shrinkage of hexagonal TiAlN and CrAlN films, Surf. Coat. Technol. 169-170, 367-370, 2003.

[55] H.C. Barshilia, N. Selvakumar, B. Deepthi, K. S. Rajam, A comparative study of reactive direct current magnetron sputtered CrAlN and CrN coatings, Surf. Coat. Technol. 201, 2193-2201, 2006.

[56] P.H. Mayrhofer, M. Geier, C. Löcker, Li Chen, Influence of deposition conditions on texture development and mechanical properties of TiN coatings, Int. J. Res. 100, 1-7, 2009.

[57] http://lb.chemie.uni-hamburg.de/

[58] G. Emig, E. Klemm, Technische Chemie, Springer Verlag, Berlin, Heidelber, 2005.

[59] N. Schalk, T. Weirather, C. Polzer, P. Polcik, C. Mitterer, A comparative study on $Ti_{1-x}Al_xN$ coatings reactively sputtered from compound and from mosaic targets, Surf. Coat. Technol. 205, 4705-4710, 2011.

[60] Y. Yamamura, H. Tawara, Energy dependence of ion-induced sputtering yields from monoatomic solids at normal incidence, Atomic Data and Nuclear Data Tables, 62, 149-253, 1996.

[61] R. Daniel, K. J. Martinschitz, J. Keckes, C. Mittere, The origin of stresses in magnetron-sputtered thin films with zone *T* structures, Acta Materialia, 2001.

[62] W. Ensinger, Ion bombardment effects during deposition of nitride and metal films, Surf. Coat. Technol. 99, 1-13, 1998.

[63] M. Hirai, Y. Ueno, T. Suzuki, W. Jiang, C. Grigoriu, K. Yatsui, Characteristics of $(Cr_{1-x}Al_x)N$ films prepared by pulsed laser deposition, Jpn. J. Appl. Phys. 40, 1056-1060, 2001.

[64] A. Reiter, AlCrN coatings: Structure, properties and application potential, PhD Thesis, Montanuniversität Leoben, 2009.

[65] D. McIntyre, J. E. Greene, Oxidation of metastable single-phase polycrystalline $Ti_{0.5}Al_{0.5}N$ films: Kinetics and mechanisms, J. Appl. Phys. 60(3), 1542-1553, 1990.

[66] R. Franz, AlCrVN-Design of high-temperature low-friction coatings, PhD Thesis, Montanuniversität Leoben, 2007.